

1 **Imprint of minute hydrocarbon seepage on solid phase and pore water**
2 **geochemistry in organic-poor subseafloor sediment**

3 Ellen Schnabel^{1*}, Jessica Stammeier², Stefanie Poetz³, Kai Mangelsdorf³, Aurèle Vuillemin¹,
4 Rolando di Primio⁴, Jens Kallmeyer¹, the PROSPECTOMICS Consortium

5 ¹GFZ Helmholtz Centre for Geosciences, Section Geomicrobiology, Telegrafenberg, 14473
6 Potsdam, Germany

7 ²GFZ Helmholtz Centre for Geosciences, Section Inorganic and Isotope Geochemistry,
8 Telegrafenberg, 14473 Potsdam, Germany

9 ³GFZ Helmholtz Centre for Geosciences, Section Organic Geochemistry, Telegrafenberg,
10 14473 Potsdam, Germany

11 ⁴AkerBP, 1366 Lysaker, Norway

12 *Corresponding author: MSc Ellen Schnabel, eschnabe@gfz.de

13 Keywords: hydrocarbon seepage; reductive diagenesis; authigenic minerals; microbial
14 activity; Barents Sea; sediment biogeochemistry

15 **Key Points**

- 16 • ~~Even inconspicuous hydrocarbon seepage modifies redox zonation and stimulates~~
17 ~~carbonate and sulfide mineral formation in marine sediments.~~Even inconspicuous
18 hydrocarbon seepage in organic-poor sediments modifies redox zonation,
19 highlighting previously unrecognized biogeochemical sensitivity in low-flux systems.
20 • Subtle seepage causes distinct spatial heterogeneity in pore water chemistry and
21 mineral formation patterns.
22 • Authigenic minerals and pore water gradients serve as complementary indicators of
23 past and ongoing seepage.

24 **Abstract**

25 In marine environments, small hydrocarbon (HC) fluxes through organic-poor sediments are
26 often fully degraded by microorganisms before reaching the seabed. Yet, these fluxes
27 influence sediment geochemistry by stimulating microbial activity. We analyzed 50 gravity
28 cores from the southwestern Barents Sea, covering zones affected by inconspicuous HC

29 seepage and unaffected reference zones. Using various organic and inorganic geochemical
30 analyses of the sediment along with pore water geochemistry, we assess the effects of low-
31 intensity seepage and identify potential geochemical signatures.

32 While analysis of the organic geochemical analyses provided limited insights, inorganic
33 geochemical analyses revealed formation of minerals such as carbonates and sulfides, linked
34 to microbial reductive processes. Element concentrations suggested that HC degradation
35 leaves distinct signatures, particularly in redox-sensitive minerals. Pore water profiles in HC-
36 affected zones showed significant variation, indicating carbonate precipitation. In contrast,
37 sediments not affected by HC seepage displayed more uniform pore water profiles.

38 Estimated fluxes of sulfate, calcium, and alkalinity varied notably between cores, particularly
39 in HC-affected zones, suggesting local and potentially transient differences in seepage
40 intensity.

41 While microbial HC degradation likely occurs deeper than our sampling interval, high-
42 resolution geochemical analysis of both sediment fractions and pore water revealed a clear
43 imprint of HC seepage. This imprint, reflected in authigenic minerals and pore water
44 gradients, allows identification of past and present seepage activity, with authigenic
45 minerals providing evidence for past seepage, and pore water profiles informing about
46 ongoing seepage.

47 **Plain language summary**

48 Hydrocarbons like methane or oil can naturally seep from underground reservoirs into
49 marine sediments. Often, this seepage is so small that hydrocarbons are fully degraded by
50 microorganisms before they reach the upper sediment layers near the seafloor.

51 In this study, we analyzed sediment from the southwestern Barents Sea, a region with very
52 low natural organic content, to investigate whether such subtle hydrocarbon seepage leaves
53 detectable traces, even when hydrocarbons are already consumed below the depth we
54 sampled.

55 Our results show that despite the complete degradation of hydrocarbons deeper in the
56 sediment, distinct changes in pore water chemistry and mineral composition persist in the
57 upper layers. We observed variations in sulfate, calcium, and alkalinity profiles, along with

58 the formation of minerals like carbonates and sulfides.

59 These findings reveal that even low-intensity hydrocarbon seepage can leave a long-lasting
60 imprint in sediments, not only through direct hydrocarbon presence, but also through their
61 impact on geochemical processes. This insight helps improving the detection of past or
62 ongoing seepage in marine environments and supports a better understanding of
63 biogeochemical cycles below the seafloor.

64 **1. Introduction**

65 Marine subseafloor biogeochemical cycles are primarily governed by microorganisms (Joye
66 et al., 2022), their metabolic activity is strongly controlled by availability and reactivity of
67 sedimentary organic substrates. Due to lesser primary productivity of surface waters as
68 compared to coastal areas (Chavez et al., 2011), in offshore sediments bioavailable organic
69 matter (OM) is typically limited and becomes more recalcitrant with burial depth
70 (Middelburg, 2018) due to lower sedimentation rates (Røy et al., 2012). However, as all
71 hydrocarbon reservoirs leak to some degree (Hunt, 1995; Heggland, 1998; Yergin, 2009),
72 underlying hydrocarbon reservoirs will lead to buoyant hydrocarbon-rich fluids migrating
73 upwards through the sediment column (Ciotoli et al., 2020). These HCs, even in trace
74 amounts, represent an additional electron donor that can significantly fuel microbial activity
75 (Zhang et al., 2022). Such influx of labile OM (i.e. seepage) leads to changes in microbial
76 communities in terms of diversity and activity, which affect in turn specific physicochemical
77 properties of the sediment, such as porosity, density, pore water geochemistry and mineral
78 composition, (Abrams, 2005; Hvoslef et al., 1996; Joye, 2020). HC seepage through marine
79 sediments fuels a variety of microbial processes, including sulfate reduction, fermentation,
80 and methanogenesis (Joye, 2020; Schnabel et al., 2025). Although these microbial processes
81 are central to *in situ* biogeochemical transformations of OM on the continental shelf
82 (Bradley et al., 2020), they are less pronounced in pelagic sediments wherein sulfate
83 reduction becomes limited due to energy limitation (Vuillemin et al., 2020). Thus, at sites
84 with low seepage rates HCs may be fully mineralized before reaching the sediment surface.
85 Nevertheless, subtle but continuous HC fluxes influence sediment geochemistry and
86 microbiology, not only in the direct vicinity of the HC source but also extending to the
87 sediment surface (Rasheed et al., 2013; Joye et al., 2004).

88 Dissimilatory sulfate reduction (DSR), which is the predominant terminal electron-accepting
89 pathway in oxygen-depleted, sulfate-containing shallow marine sediments (Kasten and
90 Jørgensen, 2000; Bowles et al., 2014; Jørgensen et al., 2019), can be expected to be
91 influenced by HC seepage and potentially be key in defining HC-related reductive diagenesis
92 (Joye et al., 2004). Organoclastic sulfate reduction (OSR) relies on low molecular weight
93 substrates derived from fermented particulate or dissolved OM (Jørgensen, 1982), whereas
94 methanotrophic sulfate reduction is performed in conjunction with methane-oxidizing
95 archaea (ANME) during anaerobic oxidation of methane (AOM) (Orphan et al., 2001). Thus,
96 the influence of HC seepage on sulfate-reducing bacteria (Widdel et al., 2010) highly
97 depends on whether light (i.e. gaseous, soluble) or heavy (i.e. long chain alkanes, aromatic
98 rings) HCs are supplied. The types of seeping HCs and their subsequent microbial alteration
99 can be resolved using mass spectrometry of sediment organic extracts, e.g. a shift from
100 polar to less polar unsaturated HCs is observed during maturation (Hu et al., 2023), whereas
101 the loss of hydrogen atoms in alkanes (via dehydrogenation) or oxygen incorporation in
102 aromatic rings (cleavage via hydroxylation) reveal subsequent microbial alteration (Sert et
103 al., 2020). Further geochemical effects inherent to sulfate reduction (SR) include an increase
104 in pore water alkalinity, primarily as dissolved inorganic carbon (DIC) in the form of
105 bicarbonate (HCO_3^-), and production of hydrogen sulfide (H_2S). Together these metabolic
106 solutes create favorable sedimentary conditions for the precipitation of carbonate and
107 sulfide minerals (Berner, 1981; Hinrichs et al., 1999; Lin et al., 2016), namely calcite (CaCO_3),
108 mackinawite (FeS) and pyrite (FeS_2). Carbonates can record redox conditions at the time of
109 formation (Vuillemin et al., 2023a and 2023b) while their trace element compositions can
110 indicate progressive alteration or diagenesis (Smrzka et al., 2019), in particular redox-
111 sensitive trace metals (Smrzka et al., 2020; Tribovillard et al., 2013). Similarly, iron sulfides
112 scavenge specific trace elements from the pore water (Huerta-Diaz and Morse, 1992),
113 including chalcophilic and redox-sensitive bioessential metals (e.g., Mn, Mo, Cu, Zn).

114 Local redox conditions mediated by microbial processes also affect HC mobility as they
115 promote the formation (e.g. carbonates) or dissolution (e.g. clays) of mineral barriers that
116 adsorb HCs or impede their diffusion (Zhao et al., 2024; Eichhubl et al., 2009). For instance,
117 the transition of smectite to illite decreases the mineral swelling capacity and reduces
118 permeability (Kim et al., 2004; Dong et al., 2009). Such interplay of physical, geochemical

119 and biological factors affects the migration of HCs and generates complex but characteristic
 120 flow patterns at active seep systems (De Groot et al., 2024). Thus, seep systems are
 121 characterized by pronounced spatial and temporal variations, permeability, fluid flow
 122 dynamics, and pressure conditions governing the rate at which HCs migrate upward (Foster
 123 et al., 2015; Leifer et al., 2004; De Groot et al., 2024), reasons for which characteristic HC
 124 seeps can be classified according to flux and surface manifestations (Table 1). Note that
 125 some seep-features like e.g. carbonate crusts or pockmarks remain even after active
 126 seepage stopped (Nickel et al. 2012, Nickel et al. 2013).

127 **Table 1.** Classification of hydrocarbon seeps based on methane flux and associated surface manifestations. The
 128 table is compiled after (Judd and Hovland (2009); Etiope (2015)). The flux range between inconspicuous- and
 129 moderate-flux seeps ($1 \text{ mmol} \times \text{m}^2 \times \text{d}^{-1}$ to $100 \text{ mmol} \times \text{m}^2 \times \text{d}^{-1}$) represents a conceptual transition zone,
 130 where current data are insufficient to establish a clear distinction.

Seep type	Inconspicuous seeps	Moderate seeps	High flux seeps
Flux range	$< 1 \text{ mmol} \times \text{m}^2 \times \text{d}^{-1}$	$0.1\text{--}1 \text{ mol} \times \text{m}^2 \times \text{d}^{-1}$	$1\text{--}10 \text{ mol} \times \text{m}^2 \times \text{d}^{-1}$
Pockmarks	No pockmarks	Small, less deeply pronounced pockmarks	Larger, deeper and more numerous pockmarks, clearer
Methane and gas bubbles	No bubbles	Few, smaller bubbles, mostly sporadic	Frequent and larger bubbles, continuous gas flow
Chemical changes	No or minimal chemical changes on the surface	Low concentration of carbonates and sulfides	Significant enrichment of carbonates and sulfides, possible mineral deposits
Biogenic hotspots	No biological hotspots	Local colonization of methane-oxidizing bacteria	Intensive biological activity, larger hotspots with more diverse methane-fed fauna (e.g. mussels)
Gas hydrates	No gas hydrates	Little or no gas hydrates	Possible presence of gas hydrates, especially at low temperatures and high methane flow

131 According to our definition inconspicuous HC seeps are seeps where the seeping HCs lack
132 visible surface manifestations. Instead, the HCs spread diffusely and are used up by
133 biogeochemical processes so that the HCs do not reach the SWI. Although they likely imprint
134 sediment geochemistry, they often remain undetected. Yet, any additional energy flux from
135 weak seepage tends to promote complex interactions among local microbial communities
136 adapted to substrate limitation or not, and influence the sediment geochemical dynamics,
137 leading to fundamental metabolic and diagenetic processes (Abrams, 2020).

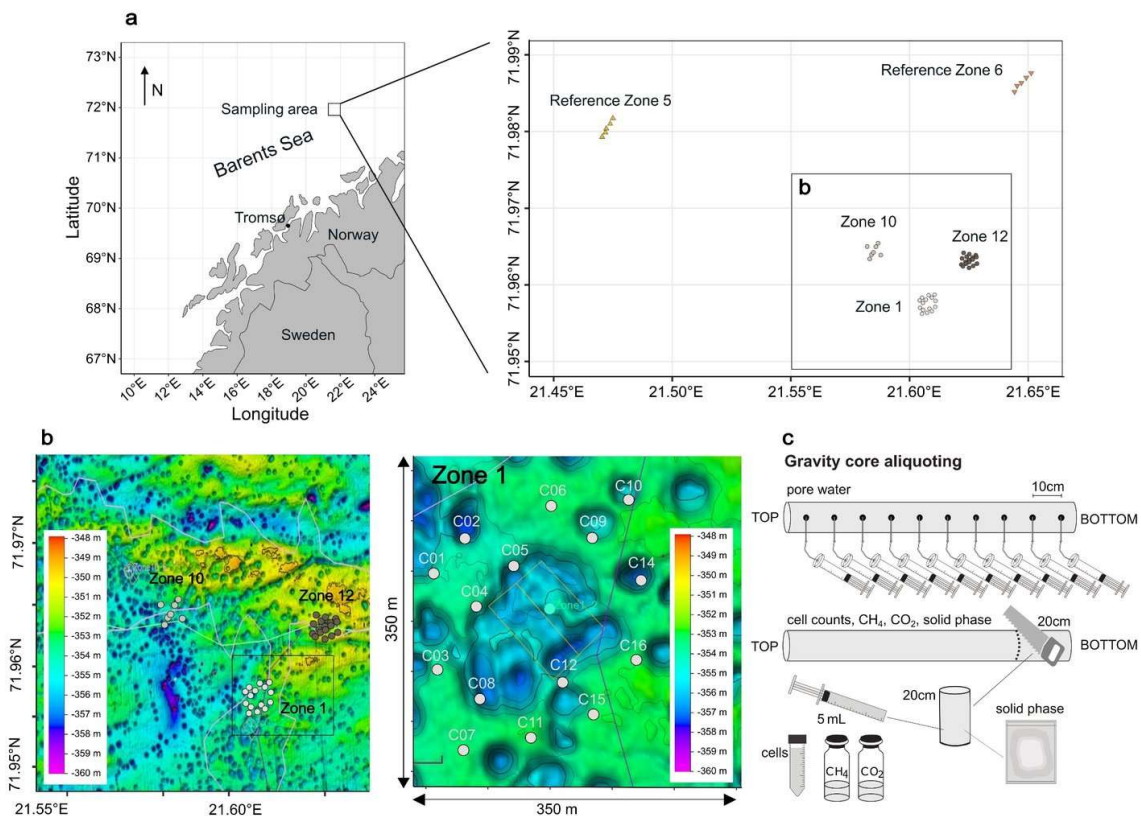
138 Here, we investigate how subtle, inconspicuous HC seepage influences the geochemical
139 composition of both pore water and sediment. We analyzed 50 gravity cores collected from
140 the southwestern Barents Sea, including 40 cores from zones affected by low-intensity
141 seepage and 10 from unaffected reference zones. Given the challenges of deeper coring and
142 the goal of minimizing environmental impact, we focused on the upper 3 meters of
143 sediment to determine whether direct or indirect effects of seepage could be detected. The
144 large number of cores allows us to identify small-scale geochemical patterns and evaluate
145 any spatial heterogeneity of discrete infiltrations. By combining organic and inorganic
146 analyses of the sediment with pore water geochemistry, we decipher (I) the extent to which
147 inconspicuous HC seeps affect the distribution of key geochemical species (e.g. sulfide,
148 methane, calcium, alkalinity) in pore water and sediment, and (II) how these parameters
149 vary spatially across and between seepage and reference zones.

150 **2. Material and Methods**

151 **2.1. Geological setting and sampling**

152 The Barents Sea is an epicontinental shelf sea bordered by the Norwegian Sea to the
153 southwest, the Arctic Ocean to the north, and the Russian archipelago of Novaya Zemlya to
154 the east. It rests on a Caledonian basement formed during Paleozoic orogenies, but its
155 present structural configuration mainly reflects Mesozoic and Cenozoic tectonic phases,
156 including episodes of uplift, subsidence, tilting, and erosion. This has resulted in a varied
157 structural landscape with elevated highs (e.g., the Loppa High) and intervening sedimentary
158 basins (Doré, 1995; Gabrielsen et al., 1990; Johansen et al., 1993; Larssen et al., 2002;
159 Faleide et al., 1984). During the Mesozoic, organic-rich marine shales were deposited under

160 greenhouse climate conditions with high marine productivity and fluctuating sea levels.
 161 These shales—particularly the Upper Jurassic Hekkingen Formation, act as the principal
 162 source rocks for hydrocarbons in the southwestern Barents Sea (Marín et al., 2020; Langrock
 163 et al., 2003). Burial over millions of years led to thermal maturation, hydrocarbon
 164 generation, and subsequent migration into structural traps, such as those found in the
 165 Johan Castberg and Snøhvit fields. In the Quaternary, the region was repeatedly covered by
 166 ice sheets. During the last glaciation, the Barents Sea was overridden by grounded ice,
 167 leading to significant glacial erosion. Consequently, the modern sediment cover on
 168 structural highs is often very thin and sediments primarily consist of glacial and glaciomarine
 169 silty clays, dropstones, and fine sands derived from the erosion of local and distal bedrock
 170 during glacial advance and retreat. These surficial sediments are typically organic-poor,
 171 reflecting both their glacial origin and limited biological productivity during deposition
 172 (Knies and Martinez, 2009; Nickel et al., 2013; Sættem et al. (1991); Elverhøi and Solheim
 173 (1983).



174
 175 **Figure 1. Sampling locations.** (a) Map of the Norwegian coast. The square marks the sampling area. Fifty cores
 176 were retrieved from three HC-affected zones (Zone 1, Zone 10, Zone 12) and two reference zones (Ref 5, Ref
 177 6). (b) Bathymetric map of the 3 HC-affected zones. Each zone was sampled in a grid of cores, Zone 1 is

178 enlarged here as an example. The missing samples in the middle are due to the increased occurrence of
 179 dropstones in this area, preventing the deployment of a gravity corer. (c) Schematic overview of the sampling
 180 strategy. This figure was modified after (Schnabel et al., 2025)

181 During an expedition to the SW Barents Sea in Oct/Nov 2021, we collected a total of fifty
 182 gravity cores, ranging from 0.5 to 3 meters in length, within three zones with known
 183 underlying HC reservoirs (Z01, Z10, Z12), as well as two zones (Ref5, Ref6) with no HC
 184 reservoirs, labelled hereafter as HC zones and reference zones (Fig. 1a). The coring sites lie
 185 at a water depth of approximately 350 meters (Fig. 1b). Immediately after retrieval of a
 186 core (Fig. 1c), the lowermost 20 cm of the core were cut off, the sediment was pushed out
 187 of the liner and the outer 1-2 cm were scraped off with a sterile spatula to remove possible
 188 contamination. Using 5 mL cut-off syringes, 3 cm³ of sediment were transferred into a 10 mL
 189 glass crimp vial containing saturated NaCl solution. The vials were immediately sealed with
 190 thick butyl rubber stoppers, crimped, and stored upside down without headspace until gas
 191 analyses in the home lab. An additional 2 cm³ of sediment was transferred into a 15 mL
 192 centrifuge tube containing 8 mL of NaCl-formalin fixative solution (25 g × L⁻¹ NaCl, 20 g × L⁻¹
 193 formalin) and thoroughly homogenized for cell counting. The remaining sediment was
 194 aliquoted for solid phase geochemistry. The rest of the core was cut into 1 m sections,
 195 capped and stored on deck, as air, water and sediment temperature were all around 5 °C.

196 Pore water was extracted on board, with extractions initiated within two hours of core
 197 retrieval. Rhizon pore water samplers (Rhizosphere Research Products B.V., Netherlands;
 198 (Seeberg-Elverfeldt et al., 2005)) were inserted into the intact sediment core through small
 199 holes drilled in ca. 10 cm intervals. Pore water collection took between 12 and 24 hours. The
 200 collected pore water samples were 0.22 µm- filtered (Merck Millex™-GS Sterile Syringe Filter
 201 Unit, MCE) and aliquoted for different downstream analyses. For anion, cation, and trace
 202 element measurements, 1.5 mL each was collected in plastic screw-cap vials without any
 203 further treatment. These samples were kept anoxic until analysis. For alkalinity
 204 measurements, 2 mL of pore water were filled into a glass vial pre-filled with 50 µL of
 205 saturated HgCl₂ solution to prevent bacterial activity (Edenborn et al., 1985) and closed
 206 without any headspace. For quantification of dissolved hydrogen sulfide, we transferred 1.5
 207 mL of pore water into a 2 mL plastic screw-cap vial and added 200 µL ZnCl₂ (20 % weight ×
 208 vol⁻¹). All samples were stored at +4 °C until analysis in the home lab.

209 2.2. Methane and carbon dioxide concentrations

210 Prior to measurement, we introduced 3 mL of ultrapure helium gas as headspace while
211 withdrawing the same amount of NaCl solution from the crimped vial. To equilibrate
212 dissolved gases with the headspace, the content of the vials was mixed at 220 rpm on an
213 orbital shaker for 18 h, and further vortexed to break up the remaining small clayey
214 aggregates. A 250 μL sample of the headspace gas was then extracted and introduced into a
215 7890A Gas Chromatography System, which was equipped with both a flame ionization
216 detector (FID) and a thermal conductivity detector (TCD), along with an HP PLOT Q column
217 (all from Agilent). The oven temperature was set to 50 $^{\circ}\text{C}$, the flow rate was maintained at
218 17.2 mL min^{-1} , and the pressure was held at 13 psi. Both detectors operated at 200 $^{\circ}\text{C}$ with
219 flow rates of 40 mL min^{-1} (FID) and 15 mL min^{-1} (TCD). Calibration of the system was
220 performed by injecting pure analytical standards with CO_2 concentrations of 310 ppm and
221 5270 ppm, as well as CH_4 concentrations of 10 ppm and 5170 ppm. The initial CH_4 and CO_2
222 concentrations were converted from ppm to molar concentrations using the ideal gas law.

223 2.3. Cell counting

224 Total cell counts were conducted following a protocol based on Kallmeyer et al. (2008).
225 Sediment samples were initially diluted at a ratio of 1:100 using a 25 g L^{-1} NaCl solution. 25
226 μL of the resulting slurry were uniformly distributed onto black 0.2 μm polycarbonate
227 Cyclopore membrane filters (Whatman International Ltd, Maidstone, UK) via vacuum
228 filtration. For cell visualization, filters were stained with a mixture consisting of SYBR Green I
229 (10 μL ; Molecular Probes, Eugene, USA), phenylenediamine (100 μL), glycerol (300 μL), Milli-
230 Q water (300 μL), and 300 μL of VECTASHIELD[®] Antifade Mounting Medium (H-1000-10,
231 Vector Laboratories, Burlingame, USA). A volume of 15 μL of this staining solution was
232 applied to each filter. The counting was performed using an epifluorescence microscope
233 (Leica DM2000, Wetzlar, Germany) by counting cells in 200 fields of view. Cell abundances
234 were calculated as \log_{10} cells per cm^3 of sediment, based on triplicate measurements, with
235 standard deviations consistently remaining below 15%.

236 2.4. Pore water geochemistry

237 Dissolved sulfate was quantified via suppressed Ion Chromatography (column: SykroGel A ×
238 300 AB-A01; eluent: 7.3 mg L⁻¹ NaSCN and 636 mg L⁻¹ NaCO₃; pump rate 1 mL min⁻¹;
239 injection volume 50 μL). The detection limit was 5 μM. Samples were measured in triplicate,
240 with average relative standard deviations consistently below 3%.

241 Cation and trace elemental concentrations in the pore water were determined using high-
242 resolution inductively coupled plasma mass spectrometry (HR-ICP-MS, ELEMENT 2XR,
243 Thermo Scientific, Waltham, USA) at the EIMiE-labs at GFZ after acidifying the samples with
244 ultrapure HNO₃ immediately prior to analysis. Until analysis, the samples were kept anoxic
245 to prevent precipitation and potential alteration of the metal concentrations. 100 μL of pore
246 water was doped with 10 μL of an indium (In) standard solution at a concentration of 100
247 μg L⁻¹ and the samples were diluted with 2 vol% ultrapure HNO₃. Trace elements were
248 quantified by external calibration using single-element standards, carefully matched to the
249 sample matrix. The acid blank was subtracted from each measurement. The detection limits
250 for the applied ICP-MS routine typically ranged between 0.5 and 1 ng g⁻¹, for the analytes.
251 Measurement uncertainty, referring to the repeatability of the measurements, was about
252 2-5 % for all analyses.

253 Iron concentrations were analyzed separately using spectrophotometry, following the
254 protocol described by Viollier et al. (2000). The detection limit of this method is 0.25 μM
255 and the measurement uncertainty was approximately 5 % for all analyses. Sulfide was
256 determined photometrically according to Cline (1969). The detection limit is 0.1 μM. All
257 samples were measured in triplicates and the results were averaged with a standard
258 deviation ≤ 3.5 %. Alkalinity was determined via titration using the Visocolor HE alkalinity AL
259 7 kit (Macherey-Nagel GmbH) adapted to the sample volume of 500 μL. The detection limit
260 is 0.15 mM and triplicate measurements differed by less than 3 %.

261 **2.5. Sediment inorganic fraction**

262 For XRF analysis, approximately 30 g of sediment material was freeze-dried, ground in agate
263 mortars using a Fritsch Pulverisette 5 planetary mill at 300 rpm for 5 minutes, sieved
264 through a 63 μm stainless steel mesh, and then melted with two Fluxana reference
265 materials to form glass discs. These discs were analyzed using an AXIOS X-ray fluorescence

266 (XRF) advanced spectrometer (Malvern Panalytical, United Kingdom), equipped with an End-
267 window RH X-ray tube SST-mAX at a 4 kW output. Elemental proportions were determined
268 for major elements as oxides in weight % [wt %] (i.e. SiO₂, Al₂O₃, Fe₂O₃, MnO, MgO, CaO,
269 Na₂O, K₂O, P₂O₅, TiO₂, SO₃, loss on ignition (LOI)), and trace elements [ppm] (i.e. Ba, Cr, Zn,
270 Ga, Nb, Ni, Rb, Sr, V, Y, Zr). Quantification limits for major elements were 0.02 wt % and
271 approximately 10 ppm for trace elements. LOI was determined based on the mass
272 difference before and after fusion. Reproducibility was evaluated using reference materials
273 and better than 2% for all major elements.

274 **2.6. Statistical and geostatistical analyses**

275 Min-max normalization was applied to the XRF dataset, scaling all variables to a range
276 between 0 and 1. PCA was then performed using the `prcomp()` function in R with centering
277 and scaling enabled to identify patterns and relationships among chemical species in the
278 solid sediment phase, reducing the data's dimensionality and highlighting key variability
279 across samples. This analysis provided further insight into the underlying structure of the
280 data, complementing the subsequent visualizations. For ternary visualization, selected
281 standardized parameters were then proportionally scaled to sum to 100 %. In some cases,
282 the resulting values of multiple compounds (e.g., those associated with specific mineral
283 groups like carbonates) were summed. Thus, the ternary diagrams reflect only relative
284 patterns and should not be interpreted in terms of absolute abundances.

285 We applied Mann–Whitney U tests (Mann and Whitney, 1947) using the function
286 `wilcox.test()` to XRF and pore water data to assess whether the median values of individual
287 chemical species differed significantly between groups. This non-parametric test was used
288 to evaluate differences in concentration gradients in the pore water and absolute
289 concentrations in the solid sediment phase between HC-affected zones (Z01, Z10, Z12) and
290 reference sites (Ref5, Ref6), as well as among and within individual zones and sediment
291 cores. To assess differences in variability (i.e. variance), we also used the Brown-Forsythe
292 test (Brown and Forsythe, 1974) applying the `leveneTest()` function . This test allowed us to
293 assess whether the variance in chemical species concentrations - reflecting chemical
294 heterogeneity - varied significantly between zones. Finally, Pearson correlation analyses
295 (Pearson, 1895; Sedgwick, 2012) were conducted on the pore water data to explore linear

296 relationships among chemical species. Two analytical levels were considered: (1)
297 correlations within individual sediment cores, and (2) correlations across all cores from the
298 same sampling zone (e.g., all cores from Z01). All statistical and geostatistical analyses were
299 performed using R version 4.2.0 (R Core Team, 2022).

300 Diffusive fluxes of sulfate, alkalinity, and calcium across the sediment–water interface were
301 calculated based on Fick's first law of diffusion using the linear concentration gradients.
302 Molecular diffusion coefficients were taken from Schulz (2006) and subsequently adjusted
303 for sediment conditions following Iversen and Jørgensen (1993). To visualize spatial patterns
304 in fluxes of sulfate, alkalinity, and calcium, we applied ordinary kriging using the `gstat`
305 package in R (Pebesma, 2004). First, empirical variograms were calculated from spatially
306 referenced flux measurements. Several theoretical variogram models (spherical,
307 exponential, Gaussian, and Matérn) were fitted and compared. The best-fitting model was
308 selected based on convergence criteria and plausibility of the sill and range parameters. This
309 model was then used to interpolate flux values across a regular spatial grid covering the
310 study area. The resulting kriging maps (Matheron, 1963) provided continuous spatial
311 representations of flux gradients and enabled the identification of heterogeneities between
312 hydrocarbon seep zones and reference sites. Visualizations were created using the `ggplot2`
313 package (Wickham, 2016).

314 **2.7. Sediment organic fraction**

315 Molecular-level insights into the organic geochemistry of sediments were obtained for
316 solvent-extractable OM using Fourier Transform Ion Cyclotron Resonance Mass
317 Spectrometry (FT-ICR-MS). Based on geochemical pore water profiles, a subset of 11
318 representative samples consisting of three samples from each of the three HC zones (Z01,
319 Z10, Z12) and one sample from each of the two reference zones (Ref5, Ref6) was selected
320 from the total of 50 sediment cores. For each sample, approximately 10 g of sediment were
321 freeze-dried, milled, and the organic content was extracted using a Soxhlet extractor
322 following a procedure described by Poetz et al. (2014). The extraction was performed with a
323 solvent mixture composed of dichloromethane and methanol (v/v = 99:1) at 40 °C for 24
324 hours. The extracts were then analyzed at ultra-high mass resolution using a Bruker Daltonik

325 Solarix 12T FT-ICR-MS. Ionization was carried out using an Apollo II ESI source and an APPI-II
326 source (all from Bruker Daltonik GmbH, Bremen, Germany).

327 For electrospray ionization (ESI⁻), nitrogen was used as the nebulizing gas at a flow rate of
328 4 L min⁻¹ at 220 °C and a pressure of 1.4 bar. The capillary voltage was set to 3000 V, and the
329 collision-induced dissociation (CID) voltage was 60 V. The samples were infused at a flow
330 rate of 2.5 µL min⁻¹ using a Hamilton syringe pump. The spectra were recorded in
331 broadband mode using 8-megaword data sets. The ion accumulation time was 0.05 s, and a
332 total of 200 scans were collected into the mass spectrum, covering a mass-to-charge ratio
333 (m/z) range of 150–1000. For atmospheric pressure photoionization (APPI⁺), nitrogen was
334 used as the nebulizing gas at a flow rate of 3 L min⁻¹ at 210 °C and a pressure of 12.3 bar.
335 The capillary voltage was set to - 1000 V, and the CID voltage was 30 V. The samples were
336 infused at a flow rate of 20 µL min⁻¹ using a Hamilton syringe pump. The spectra were
337 recorded in broadband mode using 8-megaword data sets. The ion accumulation time was
338 0.05 s, and a total of 300 scans were collected into the mass spectrum, covering an m/z
339 range of 147–1500.

340 The resulting spectra were internally recalibrated (quadratic) with a standard deviation
341 error of < 0.02 ppm, and only m/z values with a signal-to-noise ratio > 9 were exported for
342 formula assignment. Formula assignment was performed using a combination of Bruker
343 Analysis and Microsoft Excel, considering the isotopes ¹²C and ¹³C and the elemental ranges
344 C_xH_yN_{0–2}O_{0–10}S_{0–2}Na_{0–1}. The mass tolerance was set to 5 ppm.

345 **3. Results**

346 **3.1. Methane and carbon dioxide concentrations and cell abundances**

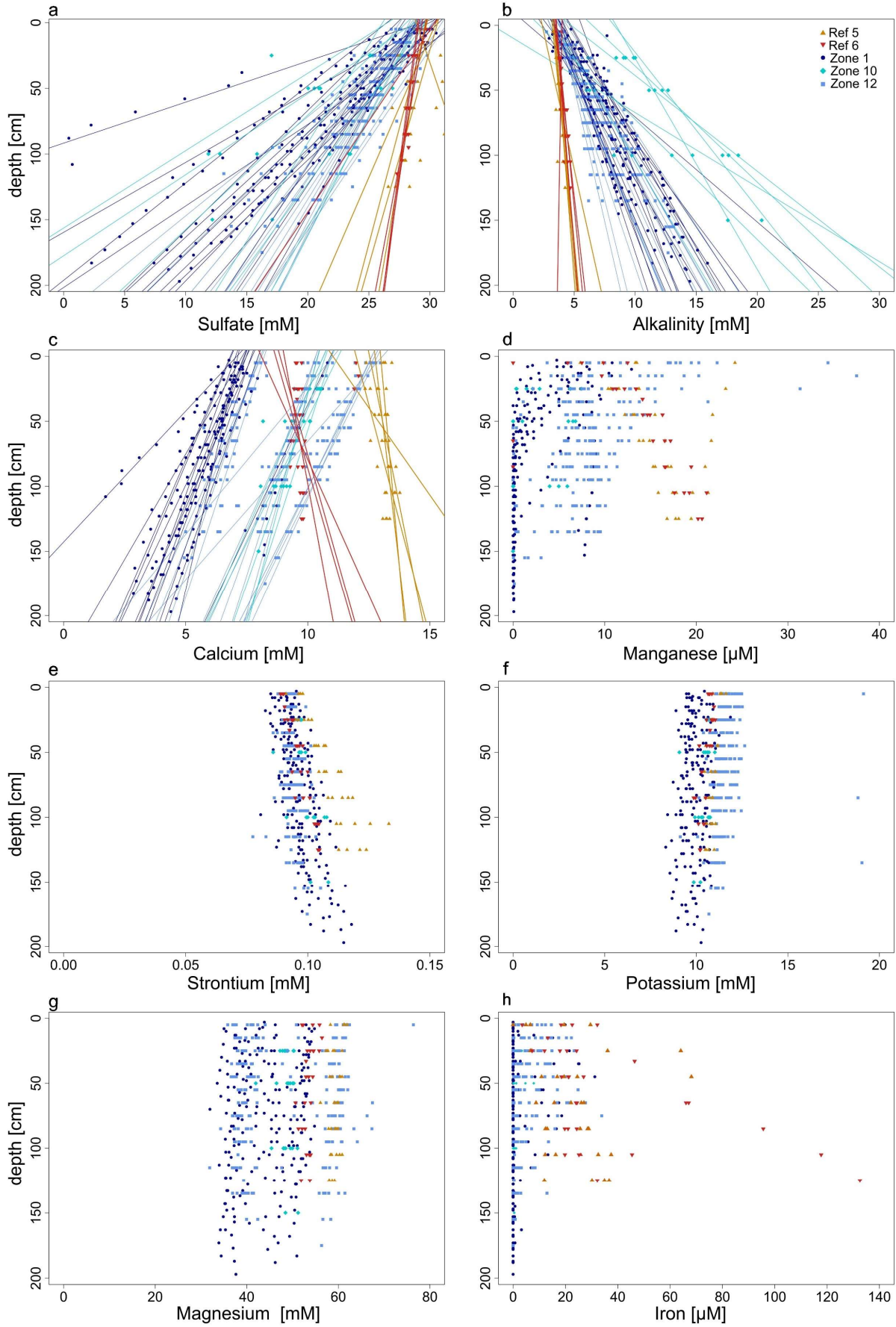
347 All samples contain measurable methane concentrations, ranging from 0.08 to 19.79 µM.
348 While samples from reference sites contain less than 5 µM of methane, higher
349 concentrations are restricted to few samples from HC-affected sites, all located deeper than
350 100 cm below seafloor (cmbsf). CO₂ was detectable in all samples, with concentrations
351 ranging from 29 µM to 512 µM, without any site-specific trend (Supplementary Fig. S1). This
352 is likely due to carbonate buffering, with dissolved CO₂ equilibrating with bicarbonate and

Imprint of minute hydrocarbon seepage on sedimentary fractions

353 carbonate in pore water at both HC-affected and reference sites. In both cases, low gas
354 concentrations prevented measurement of their stable isotopic signatures.

355 Total cell counts are approximately 10^7 cells \times cm³ across all sediment cores, with no
356 significant variation with depth (Supplementary Fig. S2). The mean deviation of cell counts
357 within samples is around 12%.

Imprint of minute hydrocarbon seepage on sedimentary fractions



358

359

Figure 2: Pore-water profiles for some representative parameters. The profiles for sulfate concentrations (a),

360 alkalinity (b), and calcium (c) show both data points and regression lines ($R^2 > 0.8$). The regression lines for HC-
 361 affected zones (Zone 1, Zone 10, Zone 12) show steeper gradients compared to those from reference zones
 362 (Ref 5, Ref 6). The profiles for magnesium (d), strontium (e), potassium (f), magnesium (g), and iron (h) are
 363 shown as data points due to the insufficient R^2 value of their respective regression lines.

364 **3.1. Pore water profiles**

365 Both sulfate and alkalinity concentrations exhibit strong linear decreasing and increasing
 366 trends ($R^2 \geq 0.85$) with depth (Figs. 2a and 2b), respectively. The gradients are steeper in the
 367 HC-affected zones compared to reference zones. Based on linear extrapolation, sulfate
 368 depletion would be reached at ca. 3 and 12 mbsf in HC and reference zones, respectively.
 369 Sulfide concentrations are below the detection limit ($1 \mu\text{M}$) in all cores from reference zones
 370 and in most of the cores from Z12 (only 2 out of 17 cores have detectable sulfide;
 371 Supplementary Fig. S3). In contrast, in most cores from Z01 (12 out of 15) and Z10 (4 out of
 372 7), sulfide concentrations increase with depth.

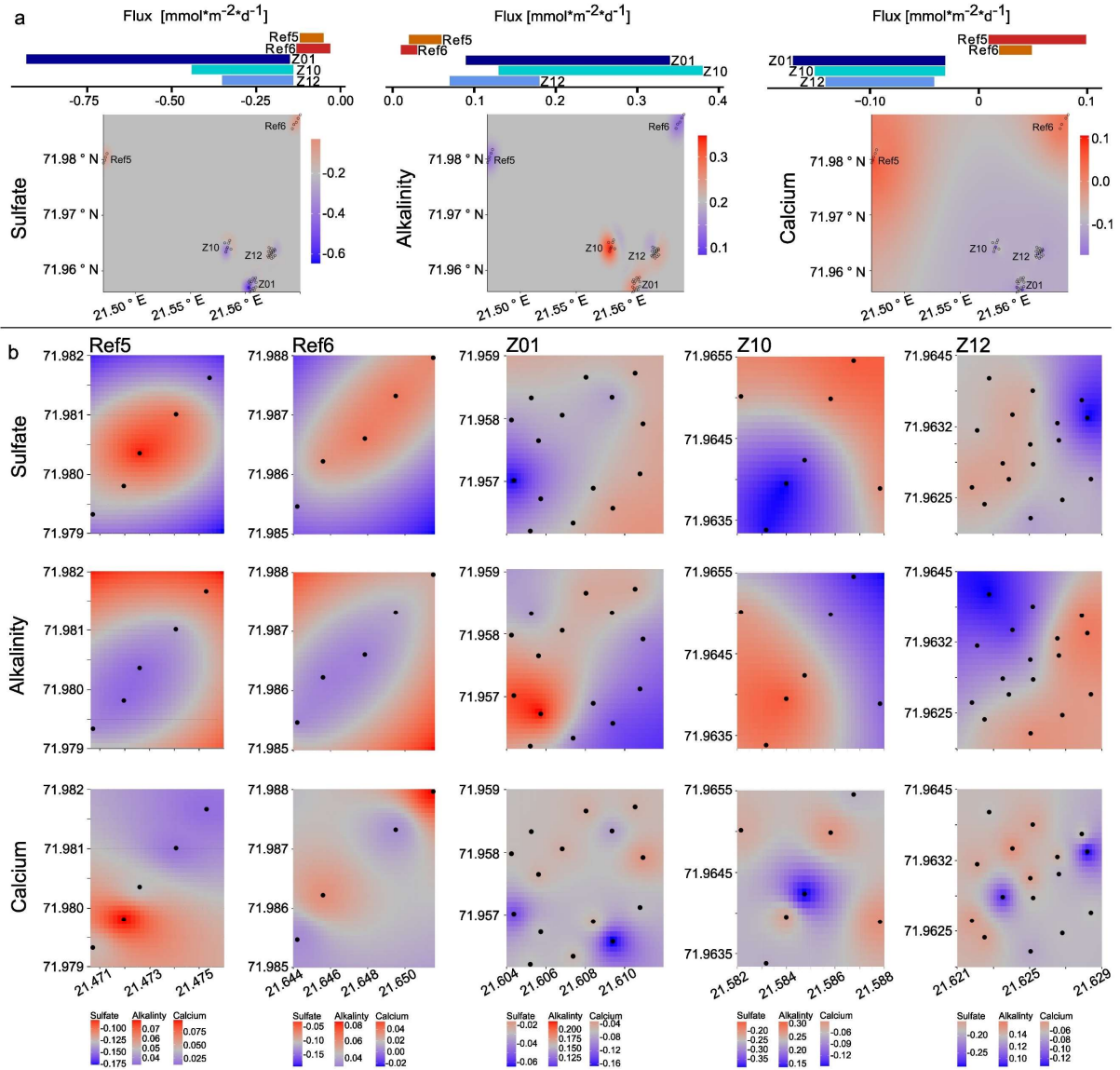
373 In the reference zones concentrations of pore water Ca^{2+} increase with depth (Fig. 2c,
 374 Supplementary Fig. S3), but decrease in the HC-affected zones. For Mn^{2+} concentrations also
 375 increase with depth in the reference zones (Fig. 2d, Supplementary Fig. S4). In most of the
 376 cores from HC-affected zones, Mn^{2+} pore water profiles show a decreasing trend with
 377 depth, but with distinct patterns, of which each one is predominant in a different sampling
 378 zone: (1) in Z01 many profiles show concentrations decreasing from ca. $15 \mu\text{M}$ at the SWI to
 379 near zero at ca. 75 cmbsf; (2) in Z12 concentrations decrease from ca. $15 \mu\text{M}$ at the SWI but
 380 then stabilize around $5 \mu\text{M}$ at 1 mbsf; (3) in Z10 and Z12 some concentrations profiles
 381 remain constant around 7 mM throughout depth.

382 Pore water concentrations for Cu^{2+} , Si^{4+} , Zn^{2+} , Mg^{2+} and K^+ remain almost unchanged in with
 383 depth in both HC-affected and reference zones (Figs. 2e-2g, Supplementary Figs. S4-S5),
 384 whereas Sr^{2+} concentrations increase in cores from both HC-affected zones and reference
 385 zones, but more pronounced for the latter (Fig. 2e). Dissolved Fe^{2+} is rarely detectable in
 386 cores from the HC-affected zones and falls below detection limit within the upper 1 mbsf
 387 (Fig. 2h). In most cores from reference zones, pore water Fe^{2+} is detectable and
 388 concentrations increase with depth. Ba^{2+} was measurable only in few cores from Z01, with

389 concentrations increasing with depth (Supplementary Fig S4). With few exceptions, Ni^{2+} and
 390 As^{2+} remain below the detection limit in all samples at all depths.

391 **3.2. Statistical analyses of inter- and intrazonal variations**

392 **3.2.1. Comparative analysis of pore water geochemistry**



393
 394 **Figure 3. Spatial variability and flux patterns of sulfate, alkalinity, and calcium across different zones.** (a) Bar
 395 plots show the mean areal fluxes ($\text{mmol}\cdot\text{m}^{-2}\cdot\text{d}^{-1}$) of sulfate (left), alkalinity (middle), and calcium (right) at the
 396 five zones (Ref5, Ref6, Z01, Z10, Z12). Kriging-interpolated maps illustrate the spatial distribution of these
 397 fluxes across the study area. Color gradients indicate the direction and magnitude of fluxes. (b) Detailed kriging
 398 maps of sulfate (top row), alkalinity (middle row), and calcium (bottom row) fluxes at each zone. Each column
 399 corresponds to one zone, showing localized spatial variability in solute fluxes. Black dots indicate the sampling
 400 sites.

401 The Mann-Whitney U tests (Mann and Whitney, 1947) confirmed statistical significance for
402 steeper sulfate and alkalinity gradients (Fig. 2, Supplementary Table S2) in HC-affected
403 zones ($p_{\text{SO}_4} = 3.86\text{E-}10$, $p_{\text{alk}} = 2.74\text{E-}05$); opposite trends in Ca^{2+} profiles ($p_{\text{Ca}} = 1.40\text{E-}04$); and
404 different pore water gradients in Mn^{2+} concentrations ($p_{\text{Mn}} = 5.38\text{E-}06$), assuming linear
405 profiles which in some cases did not provide the best fit (Fig. 2, Supplementary Fig. S4 and
406 porewater profile descriptions in Section 3.1). The results for manganese should therefore
407 be considered as approximations.

408 The Brown-Forsythe tests (Brown and Forsythe, 1974) further confirmed that the variance
409 for pore water SO_4^{2-} , alkalinity, Ca^{2+} , and Mn^{2+} gradients is smaller within reference zones
410 (all p-values < 0.05, Supplementary Table S3) than within HC-affected zones (Fig. 2). In
411 addition, a comparison of the variances across individual HC zones and reference zones
412 indicates significant differences in most instances.

413 Kriging plots for sulfate, alkalinity and calcium fluxes (which are proportional to their
414 gradients) enabled the visualization of spatial variations over the entire study area and
415 within the sampling zones (Fig. 3). The resulting patterns of variability align with previous
416 statistical tests and highlight the different spatial heterogeneity between reference and HC-
417 affected areas, with notably a stronger variability among those exposed to seepage.

418 *3.2.2. Pore water species within and across cores*

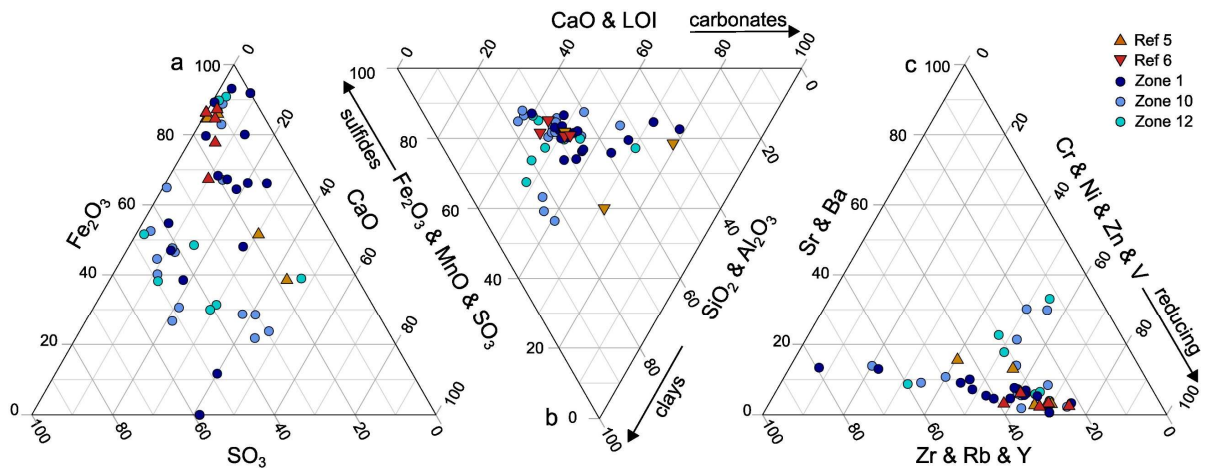
419 We also performed intra- and intervariation analyses, i.e. we investigated the correlation of
420 chemical species within each core using Pearson Correlation (Pearson, 1895; Sedgwick,
421 2012). We found a strong correlation (average $|r| > 0.86$) between sulfate, alkalinity and
422 calcium and, to a lesser extent (average $|r| > 0.66$) with manganese in almost every
423 individual core from HC zones. In contrast, within reference zones, we only found
424 correlations between alkalinity and sulfate (average $r > -0.76$) as well as alkalinity and
425 manganese (average $r > 0.86$) (Supplementary Table S4).

426 To determine whether concomitant biogeochemical processes may occur in different cores,
427 we assessed the correlation between pore water gradients for each of the 5 sampling zones
428 separately, resulting in 10 combinations of alkalinity, sulfate, manganese, calcium, and
429 sulfide. For cores from reference zones, a negative correlation between sulfate and

430 alkalinity was observed ($r = -0.80$ and -0.85 for Ref5 and Ref6). In addition, for Ref5,
 431 additional correlations were found between sulfate and manganese ($r = -0.99$), alkalinity
 432 and calcium ($r = -0.86$) and alkalinity and manganese ($r = 0.78$). For cores from the three HC
 433 HC zones, no significant correlations ($r < 0.7$) were found between geochemical species,
 434 except at Z10 between sulfate and alkalinity ($r = -0.89$), alkalinity and sulfide ($r = 0.77$)
 435 (Supplementary Table S4).

436 *3.2.3. XRF elemental concentrations of the sediment inorganic fraction*

437 CaO and SO_3 concentrations are significantly higher (Mann-Whitney U test, $p < 0.05$) in
 438 sediments from HC-affected than reference zones. Despite similar behavior as alkaline-earth
 439 elements, Ba ($p = 0.11$) and Sr ($p = 0.17$) were only slightly more abundant in sediments
 440 exposed to seepage. Conversely, the relative abundance of Fe_2O_3 , P_2O_5 , Ti, Cr, and Zn is
 441 higher ($p < 0.05$) in cores from reference zones, while Al ($p = 0.06$), Ni ($p = 0.05$), Mn ($p =$
 442 0.12), and V ($p = 0.05$) show a tendency towards higher relative abundances. The loss on
 443 ignition (LOI) is significantly higher ($p < 0.05$) in cores from reference zones.



444
 445 **Figure 4. Ternary diagrams showing the relative proportions of selected major and trace elements in solid**
 446 **phase sediments from hydrocarbon HC zones and reference zones.** (a) Major elements: Fe_2O_3 – SO_3 –CaO, (b)
 447 major elements grouped by associated mineral fractions: CaO and LOI (carbonate), Fe_2O_3 and MnO and SO_3
 448 (sulfide), and SiO_2 and Al_2O_3 (clay), and (c) trace elements grouped by geochemical behavior: Cr, Ni, Zn and V
 449 (redox-sensitive), Sr and Ba (calcite-, barite-associated), and Zr, Rb and Y (conservative). Each symbol
 450 represents an individual sample. HC zones (blue colors) and reference zones (red colors) largely overlap, the
 451 scatter in the HC zones is noticeably larger, indicating a greater variance.

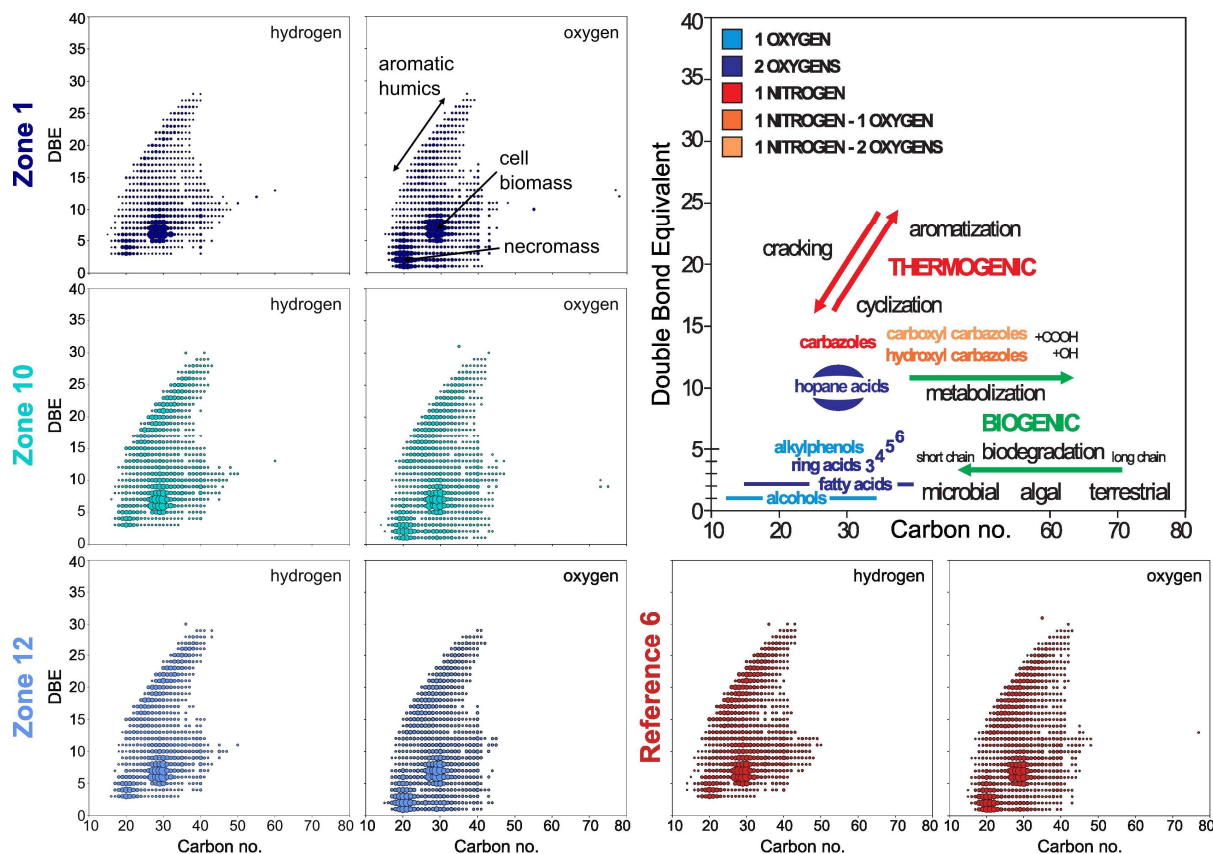
452 Significant differences ($p < 0.05$) revealed by the Brown-Forsythe variance homogeneity test
453 included Ba and SO_3 concentrations at seepage and reference zones, highlighting higher
454 variance among cores from HC-affected zones. Variance in CaO concentrations appeared
455 non-significant ($p = 0.09$). Major and trace element in ternary diagrams (Fig. 4) confirm this,
456 as the variance (scatter) is noticeably greater in the HC zones compared to the reference
457 zones. Despite considerable overlap, this observation is consistent with the results of the
458 Brown-Forsythe test, illustrating the lower variance across samples from reference zones
459 compared to HC zones. This pattern is further supported by PCA of major and trace
460 elements (Supplementary Figs. S6–S7), where samples from HC zones show greater
461 dispersion along the first principal component (60.7% and 59.8% variance explained,
462 respectively), indicating higher variability in both major and trace element composition.

463 **3.3. Organic compound classes across sampling zones**

464 The number of mass spectrometry signals and their distribution across different compound
465 classes (e.g., pure HCs, HCs with O, N, and S atoms), measured in both ionization modes
466 (APPI+ and ESI-) and analyzed in various data representations, appear very similar for both
467 seepage and reference sites. Atomic H/C and O/C ratios derived from assigned molecular
468 formulas showed no significant differences between seep and reference sites. Additionally,
469 the degree of unsaturation (i.e. double bond equivalent, DBE) relative to the number of
470 carbon atoms does not show significant variations in the relative abundance of different
471 compound classes or noticeable differences across sampling sites (Fig. 5, Supplementary Fig.
472 8).

473 Specific molecular signatures indicative of microbial biomass (e.g. hopanoids) and degraded
474 OM (e.g. humic acids) are also comparable across sampling zones (Fig. 5). Similar to total cell
475 counts, molecular clusters assigned to hopanoid-derived compounds (typically around 6–8
476 DBE and ~30 carbons) occur in similar abundance at all sites, suggesting comparable
477 microbial population sizes. Likewise, signals corresponding to fatty acids (low DBE, low
478 number of carbons), which can be interpreted as cell remnants or necromass, are evenly
479 distributed. Finally, aromatic compounds which are typically associated with humic
480 substances from highly degraded and refractory OM, are equally present in sediments from
481 all sampling zones. Signatures of seepage-related hydrocarbons, including saturated alkanes

482 and polyaromatic hydrocarbons typically associated with migrated oil and gas, were not
 483 detected.



484
 485 **Figure 5. Diagrams for molecular polar compounds identified by FT-ICR-MS in APPI+ mode in sediment**
 486 **extracts from the three hydrocarbon HC zones and one reference zone. (From left to right) Double bond**
 487 **equivalents (DBE) plotted against carbon number for compounds containing hydrogen and oxygen, and**
 488 **simplified interpretative framework of some molecular classes (e.g. aromatic acids, hopane acids,**
 489 **alkylphenols) and the expected shifts related to biogenic (e.g. microbial degradation) vs. thermogenic (e.g.**
 490 **cracking, aromatization) processes.**

491 **4. Discussion**

492 In the SW Barents Sea, sediments are particularly organic-lean, with TOC values below 0.5 %
 493 (Knies and Martinez, 2009). This low organic content enables the detection of discrete HC
 494 seeps, as even a slight supply of electron donors can result in a direct increase in the
 495 metabolic activity of HC-degrading microbial populations (Joye, 2020). This increase in
 496 metabolic activity, along with the resulting geochemical redox changes, can be distinguished
 497 from the background signal corresponding to pristine conditions at the seabed. In
 498 comparison, any microbial or geochemical signal arising from inconspicuous HC seepage in

499 organic-rich environments would be obscured by ongoing OM breakdown, hampering
500 discrimination of specific microbial populations or metabolic pathways involved in the
501 degradation of discrete HCs.

502 **4.1. Organic signatures of potentially active seepage remain elusive**

503 At seepage sites, we expected a greater diversity and higher concentrations of oxygen-
504 containing compounds in the FT-ICR-MS mass spectra due to the formation of aromatic-ring
505 radicals and by-products (e.g. alcohols, organic acids) during microbial HC degradation
506 (Radovic and Silva, 2025). In sediments not exposed to seepage, these compounds should
507 be less abundant, with overall a lower proportion of oxygenated components. However,
508 because seepage and reference sites showed similar compound class distributions (Fig. 5;
509 Supplementary Fig. S8), our data suggest that HCs had already been degraded at sediment
510 depths below the reach of our cores, or converted into compounds with chain lengths that
511 are too short for FT-ICR-MS detection. Instead, the FT-ICR-MS analysis only captured the
512 background signal of the subseafloor sediments (i.e. biomass, necromass, organic residues),
513 the corresponding compound class concentrations being consistent with similar microbial
514 cell counts across seepage and reference sites (Supplementary Fig. 2). Thus, the suitability of
515 this classical oil (and gas) analytical tool (Marshall and Rodgers, 2004) appears to be limited
516 in the context of inconspicuous seepage, indirectly supporting our basic assumption of
517 inconspicuous HC seepage in the HC-affected zones, without any indication for increased
518 microbial biomass at seep sites.

519 **4.2. Hydrocarbon seepage shapes redox zonation with precipitation of carbonate and** 520 **sulfide minerals**

521 Marine sediments exhibit a clear redox zonation, ranging from the aerobic respiration zone
522 near the surface, transiting through the nitrate, Mn^{4+} and Fe^{3+} reduction zones to the sulfate
523 reduction zone and methanogenesis (Froelich et al., 1979; Jørgensen and Kasten, 2006). In
524 the sulfate reduction zone, sulfate acts as the electron acceptor leading to the production of
525 hydrogen sulfide, bicarbonate, and water. The increase of these compounds in the pore
526 water promotes precipitation of carbonates (e.g. calcite) and sulfide minerals (e.g., pyrite)
527 (Smrzka et al., 2020; Smrzka et al., 2024; Lin et al., 2016; Peckmann et al., 2001).

528 Consequently, the incorporation of calcium, magnesium, strontium, iron, manganese, and
529 trace elements (e.g., Cu, Ni, Zn) into these minerals leads to their depletion in pore water
530 and enrichment in the sediment's inorganic fraction (Smrzka et al., 2019; Schippers and
531 Jørgensen, 2001).

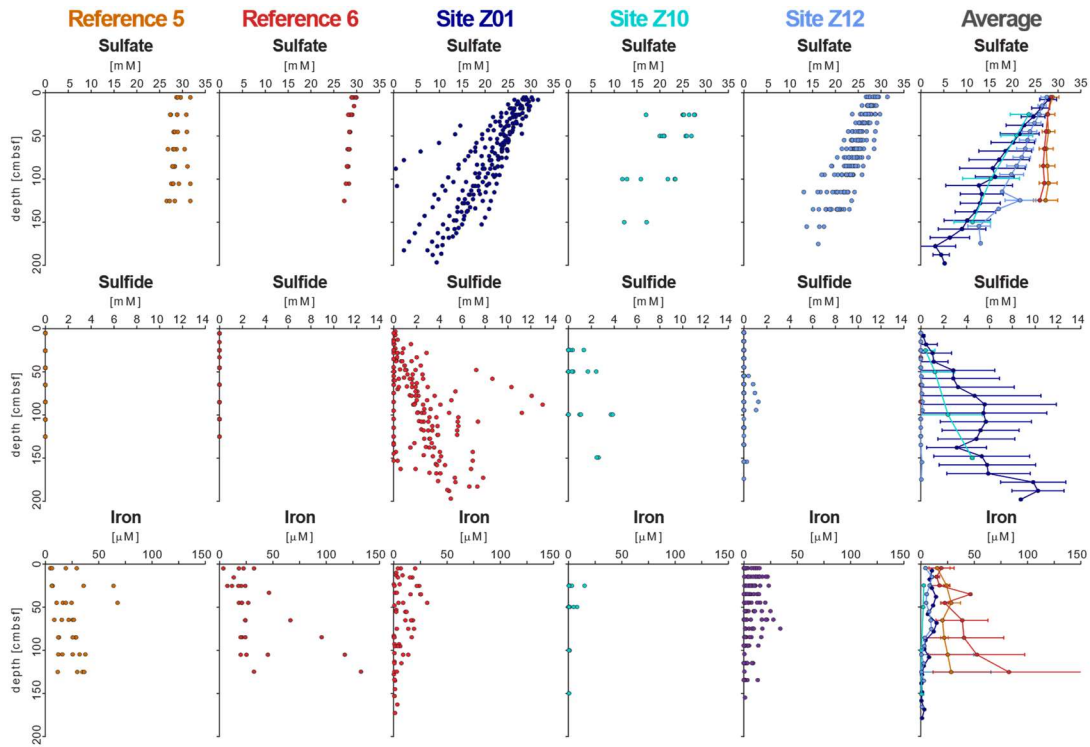
532 Both sediment geochemistry (Fig. 4, Supplementary Figs. S6-S7) and pore water analyses
533 (Fig. 2, Supplementary Figs. S3-S5) confirmed the presence of diagenetic carbonates in
534 sediments from HC zones. On the one hand, CaO, MgO, and Sr abundances increased in the
535 solid phase. On the other hand, pore water Ca²⁺ concentrations decreased while alkalinity
536 simultaneously increased with depth (Fig. 2). In contrast, Mg²⁺ and Sr²⁺ concentrations in
537 pore water remained largely unchanged. Notably, incorporation of Mg²⁺ and Sr²⁺ into
538 carbonate minerals is kinetically restricted compared to Ca²⁺ (Knight et al., 2023; Alkhatib et
539 al., 2022) and, as carbonate precipitation could occur over relatively short time periods (i.e.
540 during active seepage), substitution by pore water Mg²⁺ and Sr²⁺ appeared incomplete, thus
541 their concentrations remained almost unchanged. Although methane-derived carbonates
542 are typically high-Mg calcites or aragonite, we infer that the diagenetic carbonates in our
543 study are likely low-Mg calcites. Alternatively, the recrystallization of metastable carbonate
544 phases (e.g. aragonite) would release Sr²⁺ into the pore water (Hoareau et al., 2010). In
545 contrast to the HC zones, pore water alkalinity, Ca²⁺ and Sr²⁺ concentrations increase with
546 depth at the reference sites, while CaO and Sr contents remain low in the solid phase (Fig. 2,
547 Supplementary Fig. S3). These trends indicate that precipitation and dissolution of
548 carbonate minerals occurred (Schneider et al., 2006; Bach, 2024; Hoareau et al., 2010;
549 Smrzka et al., 2019) under seepage and non-seepage conditions, respectively.

550 Although barium (Ba²⁺) can theoretically substitute for Ca²⁺ in carbonate minerals, its larger
551 ionic radius and strong affinity for sulfate typically limit its incorporation. Instead, Ba²⁺
552 precipitates as barite (BaSO₄), which tends to dissolve under sulfate-reducing conditions
553 (Carter et al., 2020; Von Breyman et al., 1992). Indeed, Ba²⁺ was detectable in pore water
554 in only a few cores from HC-affected Zone 1 (Supplementary Fig. S4), where concentrations
555 increased with depth. This pattern suggests localized barite dissolution, likely triggered by
556 reducing conditions and upward fluid flow. Consistently, solid-phase data show elevated
557 Ba²⁺ concentrations in HC-affected zones relative to reference sites (Fig. 4, Supplementary

558 Tables S2), indicating barite accumulation through biogeochemical processes linked to HC
559 seepage. These observations highlight the dynamic interplay between sulfate availability,
560 redox zonation, and mineral precipitation at seepage sites, promoting barite formation but
561 also sulfide mineralization.

562 At seepage sites, linear profiles in pore water sulfide revealed upward diffusion
563 (Supplementary Fig. S3) and, given the low sulfate reduction rates previously measured in
564 the corresponding interval (Schnabel et al., 2025), this sulfide likely originates from deeper
565 sediment layers. When reactive metals, such as Fe^{2+} , Mn^{2+} , and other trace metals dissolved
566 in pore water, meet with ascending sulfide, precipitation of metal sulfides occurs,
567 contributing to an accumulation of redox sensitive metals and sulfur in the solid phase. This
568 is in line with observations from e.g. seeps sites in Guaymas basin (Kars et al., 2025). At
569 reference sites, dissolved sulfide is absent while Fe^{2+} and Mn^{2+} concentrations increase in
570 the pore water (Fig. 6, Supplementary Fig. S3, Supplementary Fig. S4) , suggesting that
571 anaerobic respiration of solid-phase Fe(III) and Mn(IV) oxides prevails over sulfate reduction
572 and that precipitation of metal sulfides does not take place, at least not on a quantitatively
573 significant level. Because higher pore water sulfide concentrations in our samples generally
574 correlate with elevated sulfur (i.e. SO_3) (Fig. 6) concentrations in the solid phase, sulfide
575 precipitation and sulfur accumulation allow to distinguish seepage sites from reference
576 sites, where they remain systematically low. This further demonstrates that local differences
577 in sulfide production or flux rates, as well as metal availability, may result from seepage in
578 the sediment.

Imprint of minute hydrocarbon seepage on sedimentary fractions



579

580 **Figure 6. Porewater profiles of sulfate, sulfide, and dissolved iron across five sites, including site**
 581 **averages. In seep-affected cores, iron concentrations decrease where sulfide increases, indicating**
 582 **removal of reactive iron through sulfide precipitation. Sulfate generally decreases with depth across**
 583 **all sites. Error bars represent site-specific averages where applicable.**

584 Besides major element dynamics, HC seepage also alters biogeochemical cycling of trace
 585 metals through its influence on redox zonation and authigenic mineral formation, thereby
 586 exerting control on their mobility or retention in the sediment column. Trace element
 587 incorporation into sulfide minerals vary between oil- and methane-dominated seep
 588 environments, with higher concentrations of elements like Mn, Mo, Cu, and Zn often
 589 observed in oil seep pyrites (Smrzka et al., 2024). At both seepage and reference zones,
 590 redox-sensitive trace metals (e.g. Zn, Ni, and V; Cr to a lesser extent) can be transported in
 591 solution upward from deeper sediment layers and precipitate locally depending on sulfate
 592 reduction and other redox-dependent activities. At seepage sites, methanotrophic sulfate
 593 reduction and AOM-driven processes enhance neoformation of sulfides and carbonates
 594 which act as sinks for trace metals at seep sites, in particular pyrite (Smrzka et al. (2019);
 595 Smrzka et al. (2024); Miao et al. (2022)). In contrast, lower SR activity and lesser mineral
 596 precipitation at reference sites allow trace elements to continuously diffuse upward and be
 597 captured under suboxic conditions via adsorption or precipitation as iron (oxyhydr)oxides.
 598 Altogether, despite similar concentrations in the pore fluid across sampling sites

599 (Supplementary Table S2), the degree and depth of occurrence of sulfate reduction govern
600 whether dissolved metal ions are sequestered in specific geochemical zones or bypass the
601 redox gradient. Nevertheless, trace metal concentrations may also vary with redox
602 gradients, precipitation kinetics, and phase-specific affinities (Smrzka et al. (2019),
603 hampering the use of pore water or solid phase concentration as a proxy for HC seepage.
604 Hence, a combined assessment of pore water geochemistry, redox zonation, and authigenic
605 minerals offers a more suitable approach for seepage characterization. Although our bulk
606 sediment geochemical data do not specifically target sulfide mineral phases, these findings
607 highlight the potential of geochemical signatures to record different seepage types.

608 4.3. Pore water fluxes and diagenetic minerals reflect the dynamics of transient seepage

609 Linear profiles for pore water alkalinity, SO_4^{2-} , and Ca^{2+} suggest no net turnover within the
610 sampled sediment interval (Schulz, 2006). This stands in contradiction with our observations
611 of the solid-phase geochemistry, which is indicative of carbonate and sulfide mineral
612 formation in HC-affected zones. We suggest that the sulfate-methane transition zone
613 (SMTZ), where most sulfide and carbonate precipitation occur, may have undergone
614 temporal and spatial depth fluctuations, driven by variations in HC flux over time. Such
615 fluctuations are well-documented and influenced by multiple factors, including
616 sedimentation rate, temperature, OM availability (Dale et al., 2008) and hydrostatic
617 pressure, which in the Barents Sea is particularly shaped by glacial-interglacial dynamics
618 (Argentino et al., 2021; Nickel, 2013).

619 In the Barents Sea, low sedimentation rates combined with extensive glacial history are
620 inferred to have shaped SMTZ dynamics. During the Last Glacial Maximum (~20 ka),
621 grounded ice sheets prevented seawater sulfate diffusion into the sediment in the Barents
622 Sea (Andreassen et al., 2008; Siegert et al., 2001), shifting the SMTZ upward. Following
623 deglaciation (~14 ka) (Elverhøi et al., 1993), seawater reoccupied the seafloor, restoring
624 sulfate supply and initiating a progressive downward migration of the SMTZ. Processes such
625 as gas hydrate dissociation and associated methane release during ice retreat (Nickel et al.,
626 2013) further enhanced these dynamics. Comparable patterns have been observed
627 elsewhere in the Barents Sea, where post-glacial rebound and HC flux variations have
628 caused significant SMTZ fluctuations (Argentino et al., 2021).

629 The occurrence of diagenetic carbonates and sulfides resulting most probably from past
630 AOM processes at the (paleo)SMTZ are therefore best understood as products of these
631 historical boundary conditions. Their accumulation in the sediment, in combination with
632 present-day linear pore water profiles, suggests that the system currently reflects a stage of
633 subdued seepage activity, and consequently deeper SMTZ. Thus, the present-day mineral
634 assemblage provides a cumulative archive of past seepage episodes rather than a snapshot
635 of ongoing processes, highlighting a key limitation of interpreting solid-phase geochemistry
636 alone. Although an increased presence of carbonates and sulfides may be indicative of past
637 redox conditions and fluid flow, these minerals cannot reliably distinguish active from relict
638 seepage. Integration with pore water profiles and other dynamic indicators remains
639 essential to reconstruct seepage history and assess present-day activity.

640 Overall, our findings align with typical mineralogical signatures of weak HC seeps, commonly
641 with carbonate (CaO) contents of 1-3 wt% (Rovere et al., 2020; Karaca et al., 2010) and
642 sulfur (SO₃) concentrations below 1 wt % (Fischer et al., 2012), thereby matching our
643 seepage site values (i.e. 2.1 wt% CaO, 0.8 wt% SO₃). The reference sites or our study exhibit
644 values (i.e. 1.5 wt% CaO, 0.2 wt% SO₃) that are consistent with background diagenesis
645 typically observed in non-seep environments (1–2 wt% CaO, <0.2 wt% SO₃) (Fischer et al.,
646 2012; Karaca et al., 2010). Thus, we observe that carbonate and sulfide enrichments
647 documented in Barents Sea sediments represent the imprint of past seepage episodes,
648 whereas present-day pore water profiles reflect a current state of low, or absent, HC flux
649 within the sampled interval.

650 **4.4. Fine-scale heterogeneity characterizes weak hydrocarbon seepage**

651 The HC zones are affected by inconspicuous, diffuse seepage with very low sulfate flux rates
652 below 1 mmol × m⁻² × d⁻¹ (Fig. 3). Typical fluxes at seeps range from 1–10 mol × m⁻² × d⁻¹ for
653 high flux seeps, e.g. Coal Oil Point Seep Field, Santa Barbara, California (Padilla et al., 2019),
654 and 0.1–1 mol × m⁻² × d⁻¹ for moderate flux seeps, e.g. North-western Black Sea (Hu et al.,
655 2012). Since seepage-induced biogeochemical processes, like AOM and concomitant
656 carbonate precipitation, predominantly occur below our sampling depth range (Schnabel et
657 al., 2025), their effects can be detected only indirectly. For instance, the steeper sulfate
658 gradients observed in the HC zones compared to the reference zones (Fig. 3, Supplementary

659 Fig. S3) suggest increased sulfate reduction rates due to HC supply from below. Geochemical
660 fluxes at the seepage sites show considerable variability across individual cores (Fig. 3),
661 which is considered a typical feature of seep environments inherent to localized differences
662 in fluid flow, microbial activity, or redox conditions (Pop Ristova et al., 2015; Foster et al.,
663 2015; Schnabel et al., 2025). In contrast, reference sites present rather uniform conditions,
664 as they primarily reflect sedimentation, OM input and diffusion at the sediment-water
665 interface rather than seepage.

666 In addition to variable fluxes reported for cores from seepage sites, the pattern of
667 interconnected geochemical parameters also differs on a spatial scale (Supplementary Table
668 S4). While a single pore water species may correlate in all 50 individual cores (e.g. sulfate
669 concentrations and alkalinity), ratios between parameters appear to be different for each
670 core across different HC-affected sites, and even within each individual seepage site
671 sampled. This suggests that, even though similar microbial processes (e.g. denitrification
672 reduction, sulfate reduction), can be expected to take place throughout the sampled area,
673 their degree of intensity and interactions vary on a small spatial scale, leading to
674 considerable local differences both within and between HC zones. In contrast, such
675 correlations are much better both within and across cores from reference sites (Fig. 5),
676 indicating more homogeneous and predictable diagenetic conditions.

677 **5. Conclusions**

678 This study elucidates the geochemical and mineralogical imprints of inconspicuous HC
679 seepage on near-seafloor sediments in the southwestern Barents Sea. Extremely low
680 element fluxes with often complete degradation of HCs in sediment layers below the
681 sampling depth of this study posed significant challenges in the detection of active seepage.
682 This explains why the FT-ICR-MS-based approach was unsuccessful in identifying diagnostic
683 organic compounds, as volatile and short-chained organic compounds cannot be resolved.
684 In contrast, inorganic geochemical signatures provided indirect evidence of seepage-related
685 reductive diagenetic processes. Elevated pore water alkalinity alongside decreasing Ca^{2+}
686 concentrations with depth, substantiated by elemental enrichments in the solid phase were
687 clear indications of carbonate precipitation. In addition, pore water depletion of sulfate and

688 manganese concomitant with increased solid phase sulfide concentrations point towards
689 formation of sulfide minerals. In summary, many geochemical processes along strong seeps
690 can also be directly or indirectly detected for minor HC seeps where the HCs are
691 metabolized below the sampling interval.

692 Pronounced spatial variability in geochemical gradients across seepage-affected sites was
693 observed, revealing local heterogeneity in fluid flow and redox conditions as a result of
694 variable seepage intensity. Otherwise, correlated geochemical parameters within single
695 cores pointed to consistent coupling with past and present biogeochemical processes.
696 Altogether, these spatial patterns underline the relevance of a targeted sampling strategy to
697 resolve geochemical heterogeneities in the shallow subseafloor, which proves essential for
698 capturing the transient nature of seepage. Fine-scale geochemical variations are easily
699 overlooked but are nonetheless crucial for understanding seep dynamics and differentiating
700 between active and past seepage processes, requiring adequate spatial and temporal
701 coverage and geostatistical techniques.

702 **6. Data availability**

703 The geochemical data is available on PANGAEA as dataset #974341 and #974346 under
704 digital object identifier <https://doi.pangaea.de/10.1594/PANGAEA.974341> and
705 <https://doi.pangaea.de/10.1594/PANGAEA.974346>.

706 **7. Author contributions**

707 JK and RDP organized the sampling cruise. ES and JK designed the study and collected
708 samples. ES performed cell counts and analyzed pore water geochemistry under the
709 supervision of JK. XRF measurements were performed under the supervision of JS. FT-ICR-
710 MS analyses of organic extracts were carried out by KM and SP. ES analyzed the data in
711 collaboration with AV, JK and SP. ES wrote the manuscript with input and revisions from all
712 co-authors.

713 **8. Competing interests**

714 The authors declare that they have no conflict of interest.

715 **9. Acknowledgements**

716 We thank all crew members of the RV *Sverdrup II*, Steffen Okolski, J. Axel Kitte and Edgar
 717 Kutschera for their great help during the sampling cruise. The help of Steffen Okolski in pore
 718 water analyses is acknowledged. We acknowledge the support of Anja Schleicher, Andrea
 719 Gottsche and Heike Rothe in performing the XRF and ICP-MS measurements, including
 720 sample melting and instrument operation. Sabine Kasten and Bo Liu are thanked for advices
 721 on data processing.

722 **10. Financial support**

723 This research has received funding from the European Union's Horizon 2020 research and
 724 innovation programme under grant agreement no. 899667. The article processing charge for
 725 this open-access publication were covered by GFZ Helmholtz Centre for Geosciences.

726

727 The PROSPECTOMICS Consortium

728 The principal investigators of the PROSPECTOMICS project are Jens Kallmeyer¹, Paul
 729 Wilmes², Alexander J. Probst³, Dörte Becher⁴, Thomas Rattai⁵, and Rolando di Primio⁶. The
 730 project managers are Aurèle Vuillemin¹, Cédric L. Laczny², André R. Soares³, and Anke
 731 Trautwein-Schult⁴. Scientists and technicians include Ellen Schnabel¹, Kai Mangelsdorf⁷,
 732 Steffen Okolski¹, J. Axel Kitte¹, Benoit Kunath², Zainab Zafar², Sarah Esser³, Anne Ostrzinski⁴,
 733 Sebastian Grund⁴, and Alexander Pfundner⁵.

734 ¹GFZ Helmholtz Centre for Geosciences, Section Geomicrobiology, Telegrafenberg, 14473
 735 Potsdam, Germany; ²Luxembourg Centre for Systems Biomedicine, University of
 736 Luxembourg, Esch-sur-Alzette; ³Environmental Metagenomics, Research Center One Health
 737 Ruhr of the University Alliance Ruhr, Faculty of Chemistry, University of Duisburg-Essen,
 738 Essen, Germany; ⁴Department of Microbial Proteomics, University of Greifswald, Greifswald,
 739 Germany; ⁵Computational Systems Biology, Centre for Microbiology and Environmental
 740 Systems Science, University of Vienna, Vienna, Austria; ⁶Aker BP ASA, Sandvika, Viken,

741 Norway; ⁷GFZ Helmholtz Centre for Geosciences, Section, Section Organic Geochemistry,
742 Telegrafenberg, 14473 Potsdam, Germany.

743 **11. References**

744 Abrams, M. A.: Significance of hydrocarbon seepage relative to petroleum generation and
745 entrapment, *Marine and Petroleum Geology*, 22, 457-477,
746 <https://doi.org/10.1016/j.marpetgeo.2004.08.003>, 2005.

747 Abrams, M. A.: Marine seepage variability and its impact on evaluating the surface migrated
748 hydrocarbon seep signal, *Marine and Petroleum Geology*, 121, 13,
749 <https://doi.org/10.1016/j.marpetgeo.2020.104600>, 2020.

750 Alkhatib, M., Qutob, M., Alkhatib, S., and Eisenhauer, A.: Influence of precipitation rate and
751 temperature on the partitioning of magnesium and strontium in calcite overgrowths,
752 *Chemical Geology*, 599, <https://doi.org/10.1016/j.chemgeo.2022.120841>, 2022.

753 Andreassen, K., Laberg, J. S., and Vorren, T. O.: Seafloor geomorphology of the SW Barents
754 Sea and its glaci-dynamic implications, *Geomorphology*, 97, 157-177,
755 <https://doi.org/10.1016/j.geomorph.2007.02.050>, 2008.

756 Argentino, C., Waghorn, K. A., Vadakkepuliambatta, S., Polteau, S., Bunz, S., and Panieri, G.:
757 Dynamic and history of methane seepage in the SW Barents Sea: new insights from
758 Leirdjupet Fault Complex, *Sci Rep*, 11, 4373, <https://doi.org/10.1038/s41598-021-83542-0>,
759 2021.

760 Bach, L. T.: The additionality problem of ocean alkalinity enhancement, *Biogeosciences*, 21,
761 261-277, <https://doi.org/10.5194/bg-21-261-2024>, 2024.

762 Berner, R. A.: A new geochemical classification of sedimentary environments, *Journal of*
763 *Sedimentary Research*, 51, 359-365, [https://doi.org/10.1306/212f7c7f-2b24-11d7-](https://doi.org/10.1306/212f7c7f-2b24-11d7-8648000102c1865d)
764 [8648000102c1865d](https://doi.org/10.1306/212f7c7f-2b24-11d7-8648000102c1865d), 1981.

765 Bowles, M. W., Mogollon, J. M., Kasten, S., Zabel, M., and Hinrichs, K. U.: Global rates of
766 marine sulfate reduction and implications for sub-sea-floor metabolic activities, *Science*,
767 344, 889-891, <https://doi.org/10.1126/science.1249213>, 2014.

768 Bradley, J. A., Arndt, S., Amend, J. P., Burwicz, E., Dale, A. W., Egger, M., and LaRowe, D. E.:
769 Widespread energy limitation to life in global subseafloor sediments, *Sci Adv*, 6, eaba0697,
770 <https://doi.org/10.1126/sciadv.aba0697>, 2020.

771 Brown, M. B. and Forsythe, A. B.: Robust Tests for the Equality of Variances, *Journal of the*
772 *American Statistical Association*, 69, 364-367,
773 <https://doi.org/10.1080/01621459.1974.10482955>, 1974.

- 774 Carter, S. C., Paytan, A., and Griffith, E. M.: Toward an Improved Understanding of the
775 Marine Barium Cycle and the Application of Marine Barite as a Paleoproductivity Proxy,
776 *Minerals*, 10, <https://doi.org/10.3390/min10050421>, 2020.
- 777 Chavez, F. P., Messié, M., and Pennington, J. T.: Marine primary production in relation to
778 climate variability and change, *Annual Review of Marine Science*, 3, 227–260,
779 <https://doi.org/10.1146/annurev.marine.010908.163917>, 2011.
- 780 Ciotoli, G., Procesi, M., Etiope, G., Fracassi, U., and Ventura, G.: Influence of tectonics on
781 global scale distribution of geological methane emissions, *Nat Commun*, 11, 2305,
782 <https://doi.org/10.1038/s41467-020-16229-1>, 2020.
- 783 Cline, J. D.: Spectrophotometric Determination of Hydrogen Sulfide in Natural Waters¹,
784 *Limnol Oceanogr*, 14, 454-458, <https://doi.org/10.4319/lo.1969.14.3.0454>, 1969.
- 785 Dale, A. W., Aguilera, D. R., Regnier, P., Fossing, H., Knab, N. J., and Jorgensen, B. B.:
786 Seasonal dynamics of the depth and rate of anaerobic oxidation of methane in Aarhus Bay
787 (Denmark) sediments, *Journal of Marine Research*, 66, 127-155,
788 <https://doi.org/10.1357/002224008784815775>, 2008.
- 789 de Groot, T. R., Kalenitchenko, D., Moser, M., Argentino, C., Panieri, G., Lindgren, M.,
790 Dølven, K. O., Ferré, B., Svenning, M. M., and Niemann, H.: Methanotroph activity and
791 connectivity between two seep systems north off Svalbard, *Frontiers in Earth Science*, 12,
792 <https://doi.org/10.3389/feart.2024.1287226>, 2024.
- 793 Dong, H., Jaisi, D. P., Kim, J., and Zhang, G.: Microbe-clay mineral interactions, *American*
794 *Mineralogist*, 94, 1505-1519, <https://doi.org/10.2138/am.2009.3246>, 2009.
- 795 Doré, A. G.: Barents Sea Geology, Petroleum Resources and Commercial Potential, *ARCTIC*,
796 48, 207-221, 1995.
- 797 Edenborn, H. M., Paquin, Y., and Chateauneuf, G.: Bacterial contribution to manganese
798 oxidation in a deep coastal sediment, *Estuarine, Coastal and Shelf Science*, 21, 801-815,
799 [https://doi.org/10.1016/0272-7714\(85\)90074-5](https://doi.org/10.1016/0272-7714(85)90074-5), 1985.
- 800 Eichhubl, P., Davatzes, N. C., and Becker, S. P.: Structural and diagenetic control of fluid
801 migration and cementation along the Moab fault, Utah, *Aapg Bulletin*, 93, 653-681,
802 <https://doi.org/10.1306/02180908080>, 2009.
- 803 Elverhøi, A. and Solheim, A.: The Barents Sea ice sheet - a sedimentological discussion, *Polar*
804 *Research*, 1, 23-42, <https://doi.org/10.1111/j.1751-8369.1983.tb00729.x>, 1983.
- 805 Elverhøi, A., Fjeldskaar, W., Solheim, A., Nyland-Berg, M., and Russwurm, L.: The Barents Sea
806 Ice Sheet - a model of its growth and decay during the last ice maximum, *Quaternary*
807 *Science Reviews*, 12, 11, [https://doi.org/10.1016/0277-3791\(93\)90025-H](https://doi.org/10.1016/0277-3791(93)90025-H), 1993.
- 808 Etiope, G.: *Natural Gas Seepage- The Earth's Hydrocarbon Degassing*, Springer, ISBN 978-3-
809 319-14601-0, 2015.

- 810 Faleide, J. I., Gudlaugsson, S. T., and Jacquart, G.: Evolution of the western Barents Sea,
 811 Marine and Petroleum Geology, 1, 123-150, [https://doi.org/10.1016/0264-8172\(84\)90082-](https://doi.org/10.1016/0264-8172(84)90082-5)
 812 5, 1984.
- 813 Fischer, D., Sahling, H., Nöthen, K., Bohrmann, G., Zabel, M., and Kasten, S.: Interaction
 814 between hydrocarbon seepage, chemosynthetic communities, and bottom water redox at
 815 cold seeps of the Makran accretionary prism: insights from habitat-specific pore water
 816 sampling and modeling, Biogeosciences, 9, 2013-2031, [https://doi.org/10.5194/bg-9-2013-](https://doi.org/10.5194/bg-9-2013-2012)
 817 2012, 2012.
- 818 Foster, K. L., Stern, G. A., Carrie, J., Bailey, J. N., Outridge, P. M., Sanei, H., and Macdonald, R.
 819 W.: Spatial, temporal, and source variations of hydrocarbons in marine sediments from
 820 Baffin Bay, Eastern Canadian Arctic, Sci Total Environ, 506-507, 430-443,
 821 <https://doi.org/10.1016/j.scitotenv.2014.11.002>, 2015.
- 822 Froelich, P. N., Klinkhammer, G. P., Bender, M. L., Luedtke, N. A., Heath, G. R., Cullen, D.,
 823 Dauphin, P., Hammond, D., Hartman, B., and Maynard, V.: Early oxidation of organic matter
 824 in pelagic sediments of the eastern equatorial Atlantic: suboxic diagenesis, Geochimica et
 825 Cosmochimica Acta, 43, 1975-1090, [https://doi.org/10.16/0016-7037\(79\)90095-4](https://doi.org/10.16/0016-7037(79)90095-4), 1979.
- 826 Gabrielsen, R. H., Faerseth, R. B., Jensen, L. N., Kalheim, J. E., and Riis, F.: Structural elements
 827 of the Norwegian continental shelf, Part 1: The Barents Sea Region, NPD Bulletin, 6, 1-33,
 828 1990.
- 829 Heggland, R.: Gas seepage as an indicator of deeper prospective reservoirs. A study based
 830 on exploration 3D seismic data, Marine and Petroleum Geology, 15, 1-9,
 831 [https://doi.org/10.1016/S0264-8172\(97\)00060-3](https://doi.org/10.1016/S0264-8172(97)00060-3), 1998.
- 832 Hinrichs, K. U., Hayes, J. M., Sylva, S. P., Brewer, P. G., and DeLong, E. F.: Methane-
 833 consuming archaeobacteria in marine sediments, Nature, 398, 802-805,
 834 <https://doi.org/10.1038/19751>, 1999.
- 835 Hoareau, G., Monnin, C., and Odonne, F.: A study of celestine equilibrium in marine
 836 sediments using the entire ODP/IODP porewater data base, Geochimica et Cosmochimica
 837 Acta, 74, 3925-3937, <https://doi.org/10.1016/j.gca.2010.03.033>, 2010.
- 838 Hu, L., Yvon-Lewis, S. A., Kessler, J. D., and MacDonald, I. R.: Methane fluxes to the
 839 atmosphere from deepwater hydrocarbon seeps in the northern Gulf of Mexico, Journal of
 840 Geophysical Research: Oceans, 117, <https://doi.org/10.1029/2011jc007208>, 2012.
- 841 Hu, T., Luo, M., Qi, Y., He, D., Chen, L., Xu, Y., and Chen, D.: Molecular evidence for the
 842 production of labile, sulfur-bearing dissolved organic matter in the seep sediments of the
 843 South China Sea, Water Res, 233, 119732, <https://doi.org/10.1016/j.watres.2023.119732>,
 844 2023.
- 845 Huerta-Diaz, M. A. and Morse, J. W.: Pyritization of trace metals in anoxic marine sediments,
 846 Geochimica et Cosmochimica Acta, 56, 2681-2702, [https://doi.org/10.1016/0016-](https://doi.org/10.1016/0016-7037(92)90353-k)
 847 7037(92)90353-k, 1992.

- 848 Hunt, J. M.: *Petroleum Geochemistry and Geology*, W.H.Freeman & Co Ltd, New York, ISBN
849 9780716724414, 1995.
- 850 Hvoslef, S., Christie, O. H. J., Sassen, R., Kennicutt, M. C., Requejo, A. G., and Brooks, J. M.:
851 Test of a new surface geochemistry tool for resource prediction in frontier areas, *Marine*
852 *and Petroleum Geology*, 13, 107-124, [https://doi.org/10.1016/0264-8172\(95\)00032-1](https://doi.org/10.1016/0264-8172(95)00032-1), 1996.
- 853 Iversen, N. and Jørgensen, B. B.: Diffusion coefficients of sulfate and methane in marine
854 sediments: Influence of porosity, *Geochemica et Cosmochemica Acta*, 57, 571-778,
855 [https://doi.org/10.1016/0016-7037\(93\)90368-7](https://doi.org/10.1016/0016-7037(93)90368-7), 1993.
- 856 Johansen, S. E., Ostist, B. K., Birkeland, Ø., Fedorovsky, Y. F., Martirosjan, V. N., Bruun
857 Christensen, O., Cheredeev, S. I., Ignatenko, E. A., and Margulis, L. S.: Hydrocarbon potential
858 in the Barents Sea region: play distribution and potential, *Norwegian Petroleum Society*
859 *Special Publications*, 2, 273-320, <https://doi.org/10.1016/B978-0-444-88943-0.50024-1>,
860 1993.
- 861 Jørgensen, B. B.: Mineralization of organic matter in the sea bed—the role of sulphate
862 reduction, *Nature*, 296, 643-645, <https://doi.org/10.1038/296643a0>, 1982.
- 863 Jørgensen, B. B. and Kasten, S.: Sulfur Cycling and Methane Oxidation, in: *Marine*
864 *Geochemistry*, 271-309, https://doi.org/10.1007/3-540-32144-6_8, 2006.
- 865 Jørgensen, B. B., Findlay, A. J., and Pellerin, A.: The Biogeochemical Sulfur Cycle of Marine
866 Sediments, *Front Microbiol*, 10, 849, <https://doi.org/10.3389/fmicb.2019.00849>, 2019.
- 867 Joye, S. B.: The Geology and Biogeochemistry of Hydrocarbon Seeps, *Annual Review of Earth*
868 *and Planetary Sciences*, 48, 205-231, [https://doi.org/10.1146/annurev-earth-063016-](https://doi.org/10.1146/annurev-earth-063016-020052)
869 [020052](https://doi.org/10.1146/annurev-earth-063016-020052), 2020.
- 870 Joye, S. B., Bowles, M. W., and Ziervogel, K.: Marine Biogeochemical Cycles, in: *The Marine*
871 *Microbiome*, 623-671, https://doi.org/10.1007/978-3-030-90383-1_15, 2022.
- 872 Joye, S. B., Boetius, A., Orcutt, B. N., Montoya, J. P., Schulz, H. N., Erickson, M. J., and Lugo,
873 S. K.: The anaerobic oxidation of methane and sulfate reduction in sediments from Gulf of
874 Mexico cold seeps, *Chemical Geology*, 205, 219-238,
875 <https://doi.org/10.1016/j.chemgeo.2003.12.019>, 2004.
- 876 Judd, A. and Hovland, M.: *Seabed fluid flow- The impact on geology, biology and the marine*
877 *environment*, Cambridge University Press, <https://doi.org/10.1017/cbo9780511535918>,
878 2009.
- 879 Kallmeyer, J., Smith, D. C., Spivack, A. J., and D'Hondt, S.: New cell extraction procedure
880 applied to deep subsurface sediments, *Limnology and Oceanography: Methods*, 6, 236-245,
881 <https://doi.org/10.4319/lom.2008.6.236>, 2008.
- 882 Karaca, D., Hensen, C., and Wallmann, K.: Controls on authigenic carbonate precipitation at
883 cold seeps along the convergent margin off Costa Rica, *Geochemistry, Geophysics,*
884 *Geosystems*, 11, <https://doi.org/10.1029/2010gc003062>, 2010.

- 885 Kars, M. A. C., Pastor, L., Burin, C., and Koornneef, L. M. T.: Data report: characterization of
 886 iron oxides and iron sulfides in sediments from IODP Expedition 385 Sites U1549 and U1552
 887 using rock magnetism and geochemistry, in: Proceedings of the International Ocean
 888 Discovery Program, Teske, A., Lizarralde, D., Höfig, T. W., and the Expedition 385 Scientists
 889 (Eds.), Volume 385, 19 pp., International Ocean Discovery Program,
 890 <https://doi.org/10.14379/iodp.proc.385.207.2025>, 2025.
- 891 Kasten, S. and Jørgensen, B. B.: Sulfate Reduction in Marine Sediments, in: Marine
 892 Geochemistry, Springer, Heidelberg, 263-281, [https://doi.org/10.1007/978-3-662-04242-](https://doi.org/10.1007/978-3-662-04242-7_8)
 893 [7_8](https://doi.org/10.1007/978-3-662-04242-7_8), 2000.
- 894 Kim, J., Dong, H. L., Seabaugh, J., Newell, S. W., and Eberl, D. D.: Role of microbes in the
 895 smectite-to-illite reaction, *Science*, 303, 830-832, <https://doi.org/10.1126/science.1093245>,
 896 2004.
- 897 Knies, J. and Martinez, P.: Organic matter sedimentation in the western Barents Sea region:
 898 Terrestrial and marine contribution based on isotopic composition and organic nitrogen
 899 content, *Norwegian Journal of Geology*, 89, 79-89, 2009.
- 900 Knight, A. W., Harvey, J. A., Shohel, M., Lu, P., Cummings, D., and Ilgen, A. G.: The combined
 901 effects of Mg²⁺ and Sr²⁺ incorporation during CaCO₃ precipitation and crystal growth,
 902 *Geochimica et Cosmochimica Acta*, 345, 16-33, <https://doi.org/10.1016/j.gca.2023.01.021>,
 903 2023.
- 904 Langrock, U., Stein, R., Lipinski, M., and Brumsack, H.-J. r.: Paleoenvironment and sea-level
 905 change in the early Cretaceous Barents Sea? implications from near-shore marine sapropels,
 906 *Geo-Marine Letters*, 23, 34-42, <https://doi.org/10.1007/s00367-003-0122-5>, 2003.
- 907 Larssen, G. B., Elvebakk, G., Henriksen, L. B., Kristensen, S.-E., Nilsson, I., Samuelsen, T. J.,
 908 Svana, T. A., Stemmerik, L., and Worsley, D.: Upper Palaeozoic lithostratigraphy of the
 909 Southern Norwegian Barents Sea, *Norsk Geologisk Undersøkelser, Bull.*, 444, 43, 2002.
- 910 Leifer, I., Boles, J. R., Luyendyk, B. P., and Clark, J. F.: Transient discharges from marine
 911 hydrocarbon seeps: spatial and temporal variability, *Environmental Geology*, 46, 1038-1052,
 912 <https://doi.org/10.1007/s00254-004-1091-3>, 2004.
- 913 Lin, Z., Sun, X., Peckmann, J., Lu, Y., Xu, L., Strauss, H., Zhou, H., Gong, J., Lu, H., and Teichert,
 914 B. M. A.: How sulfate-driven anaerobic oxidation of methane affects the sulfur isotopic
 915 composition of pyrite: A SIMS study from the South China Sea, *Chemical Geology*, 440, 26-
 916 41, <https://doi.org/10.1016/j.chemgeo.2016.07.007>, 2016.
- 917 Mann, H. B. and Whitney, D. R.: On a Test of Whether one of Two Random Variables is
 918 Stochastically Larger than the Other, *The Annals of Mathematical Statistics*, 18, 50-60,
 919 <https://doi.org/10.1214/aoms/1177730491>, 1947.
- 920 Marín, D., Hellenen, S., Escalona, A., Olausson, S., Cedeño, A., Nøhr-Hansen, H., and Ohm, S.:
 921 The Middle Jurassic to lowermost Cretaceous in the SW Barents Sea: Interplay between

- 922 tectonics, coarse-grained sediment supply and organic matter preservation, *Basin Research*,
 923 33, 1033-1055, <https://doi.org/10.1111/bre.12504>, 2020.
- 924 Marshall, A. G. and Rodgers, R. P.: Petroleomics: the next grand challenge for chemical
 925 analysis, *Acc Chem Res*, 37, 53-59, <https://doi.org/10.1021/ar020177t>, 2004.
- 926 Matheron, G.: Principles of geostatistics, *Economic Geology*, 58, 1246-1266,
 927 <https://doi.org/10.2113/gsecongeo.58.8.1246>, 1963.
- 928 Miao, X., Feng, X., Li, J., Liu, X., Liang, J., Feng, J., Xiao, Q., Dan, X., and Wei, J.: Enrichment
 929 mechanism of trace elements in pyrite under methane seepage, *Geochemical Perspectives*
 930 *Letters*, 21, 18-22, <https://doi.org/10.7185/geochemlet.2211>, 2022.
- 931 Middelburg, J. J.: Reviews and syntheses: to the bottom of carbon processing at the
 932 seafloor, *Biogeosciences*, 15, 413-427, <https://doi.org/10.5194/bg-15-413-2018>, 2018.
- 933 Nickel, J. C., di Primio, R., Mangelsdorf, K., Stoddart, D., and Kallmeyer, J.: Characterization
 934 of microbial activity in pockmark fields of the SW-Barents Sea, *Marine Geology*, 332–334,
 935 152–162, <https://doi.org/10.1016/j.margeo.2012.02.002>, 2012.
- 936 Nickel, J. C., di Primio, R., Kallmeyer, J., Hammer, Ø., Horsfield, B., Stoddart, D., Brunstad, H.,
 937 and Mangelsdorf, K.: Tracing the origin of thermogenic hydrocarbon signals in pockmarks
 938 from the southwestern Barents Sea, *Organic Geochemistry*, 63, 73-84,
 939 <https://doi.org/10.1016/j.orggeochem.2013.08.008>, 2013.
- 940 Orphan, V. J., Hinrichs, K. U., Ussler, W., 3rd, Paull, C. K., Taylor, L. T., Sylva, S. P., Hayes, J.
 941 M., and Delong, E. F.: Comparative analysis of methane-oxidizing archaea and sulfate-
 942 reducing bacteria in anoxic marine sediments, *Appl Environ Microbiol*, 67, 1922-1934,
 943 <https://doi.org/10.1128/AEM.67.4.1922-1934.2001>, 2001.
- 944 Padilla, A. M., Loranger, S., Kinnaman, F. S., Valentine, D. L., and Weber, T. C.: Modern
 945 Assessment of Natural Hydrocarbon Gas Flux at the Coal Oil Point Seep Field, Santa Barbara,
 946 California, *Journal of Geophysical Research: Oceans*, 124, 2472-2484,
 947 <https://doi.org/10.1029/2018jc014573>, 2019.
- 948 Pearson, K.: Note on regression and inheritance in the case of two parents, *Proceedings of*
 949 *the Royal Society of London*, 58, 240-242, <https://doi.org/10.1098/rspl.1895.0041>, 1895.
- 950 Pebesma, E. J.: Multivariable geostatistics in S: the gstat package, *Computers & Geosciences*,
 951 30, 683-691, <https://doi.org/10.1016/j.cageo.2004.03.012>, 2004.
- 952 Peckmann, J., Reimer, A., Luth, U., Luth, C., Hansen, B. T., Heinicke, C., Hoefs, J., and Reitner,
 953 J.: Methane-derived carbonates and authigenic pyrite from the northwestern Black Sea,
 954 *Marine Geology*, 177, 129-150, [https://doi.org/10.1016/S0025-3227\(01\)00128-1](https://doi.org/10.1016/S0025-3227(01)00128-1), 2001.
- 955 Poetz, S., Horsfield, B., and Wilkes, H.: Maturity-Driven Generation and Transformation of
 956 Acidic Compounds in the Organic-Rich Posidonia Shale as Revealed by Electrospray
 957 Ionization Fourier Transform Ion Cyclotron Resonance Mass Spectrometry, *Energy & Fuels*,
 958 28, 4877-4888, <https://doi.org/10.1021/ef500688s>, 2014.

- 959 Pop Ristova, P., Wenzhofer, F., Ramette, A., Felden, J., and Boetius, A.: Spatial scales of
 960 bacterial community diversity at cold seeps (Eastern Mediterranean Sea), *ISME J*, 9, 1306-
 961 1318, <https://doi.org/10.1038/ismej.2014.217>, 2015.
- 962 R: A language and environment for statistical computing: <https://www.R-project.org/>, last
 963 access: 2023-06-12.
- 964 Radovic, J. R. and Silva, R. C.: Ultrahigh-Resolution Mass Spectrometry Advances for
 965 Biogeochemical Analysis: From Seafloor Sediments to Petroleum and Marine Oil Spills, *J Am
 966 Soc Mass Spectrom*, 36, 7-33, <https://doi.org/10.1021/jasms.4c00266>, 2025.
- 967 Rasheed, M. A., Lakshmi, M., Rao, P. L. S., Kalpana, M. S., Dayal, A. M., and Patil, D. J.:
 968 Geochemical evidences of trace metal anomalies for finding hydrocarbon microseepage in
 969 the petroliferous regions of the Tatipaka and Pasarlapudi areas of Krishna Godavari Basin,
 970 India, *Petroleum Science*, 10, 19-29, <https://doi.org/10.1007/s12182-013-0245-x>, 2013.
- 971 Rovere, M., Mercorella, A., Frapiccini, E., Funari, V., Spagnoli, F., Pellegrini, C., Bonetti, A. S.,
 972 Veneruso, T., Tassetti, A. N., Dell'Orso, M., Mastroianni, M., Giuliani, G., De Marco, R., Fabi,
 973 G., Ciccone, F., and Antoncecchi, I.: Geochemical and Geophysical Monitoring of
 974 Hydrocarbon Seepage in the Adriatic Sea, *Sensors (Basel)*, 20,
 975 <https://doi.org/10.3390/s20051504>, 2020.
- 976 Røy, H., Kallmeyer, J., Adhikari, R. R., Pockalny, R., Jørgensen, B. B., and D'Hondt, S.: Aerobic
 977 microbial respiration in 86-million-year-old deep-sea red clay, *Science*, 336, 922-925,
 978 <https://doi.org/10.1126/science.1219424>, 2012.
- 979 Sættem, J., Rise, L., and Westgaard, D. A.: Composition and properties of glacial
 980 sediments in the southwestern Barents Sea, *Marine Geotechnology*, 10, 229-255,
 981 <https://doi.org/10.1080/10641199109379893>, 1991.
- 982 Schippers, A. and Jørgensen, B. B.: Oxidation of pyrite and iron sulfide by manganese dioxide
 983 in marine sediments, *Geochimica et Cosmochimica Acta*, 65, 915-922,
 984 [https://doi.org/10.1016/s0016-7037\(00\)00589-5](https://doi.org/10.1016/s0016-7037(00)00589-5), 2001.
- 985 Schnabel, E., Vuillemin, A., Laczny, C. C., Kunath, B. J., Soares, A. R., Probst, A. J., Di Primio,
 986 R., Kallmeyer, J., and the, P. C.: Influence of minor hydrocarbon seepage on sulfur cycling in
 987 marine subsurface sediments, *Biogeosciences*, 22, 767-784, <https://doi.org/10.5194/bg-22-767-2025>, 2025.
- 989 Schneider, R. R., Schulz, H. D., and Hensen, C.: Marine Carbonates: Their Formation and
 990 Destruction, in: *Marine Geochemistry*, edited by: Schulz, H. D., and Zabel, M., Springer,
 991 Berlin, Heidelberg, 311-337, https://doi.org/10.1007/3-540-32144-6_9, 2006.
- 992 Schulz, H. D.: Quantification of Early Diagenesis: Dissolved Constituents in Pore Water and
 993 Signals in the Solid Phase, in: *Marine Geochemistry*, 73-124, https://doi.org/10.1007/3-540-32144-6_3, 2006.
- 995 Sedgwick, P.: Pearson's correlation coefficient, *Bmj*, 345, e4483-e4483,
 996 <https://doi.org/10.1136/bmj.e4483>, 2012.

- 997 Seeberg-Elverfeldt, J., Schluter, M., Feseker, T., and Kolling, M.: Rhizon sampling of
 998 porewaters near the sediment-water interface of aquatic systems, *Limnol Oceanogr-Meth*,
 999 3, 361-371, <https://doi.org/10.4319/lom.2005.3.361>, 2005.
- 1000 Sert, M. F., D'Andrilli, J., Gründger, F., Niemann, H., Granskog, M. A., Pavlov, A. K., Ferré, B.,
 1001 and Silyakova, A.: Compositional Differences in Dissolved Organic Matter Between Arctic
 1002 Cold Seeps Versus Non-Seep Sites at the Svalbard Continental Margin and the Barents Sea,
 1003 *Frontiers in Earth Science*, 8, <https://doi.org/10.3389/feart.2020.552731>, 2020.
- 1004 Siegert, M. J., Dowdeswell, J. A., Hald, M., and Svendsen, J. I.: Modelling the Eurasian Ice
 1005 Sheet through a full (Weichselian) glacial cycle, *Global and Planetary Change*, 31, 367-385,
 1006 [https://doi.org/10.1016/S0921-8181\(01\)00130-8](https://doi.org/10.1016/S0921-8181(01)00130-8), 2001.
- 1007 Smrzka, D., Lin, Z., Monien, P., Chen, T., Bach, W., Peckmann, J., and Bohrmann, G.: Pyrite-
 1008 based trace element fingerprints for methane and oil seepage, *Geochemical Perspectives*
 1009 *Letters*, 29, 33-37, <https://doi.org/10.7185/geochemlet.2409>, 2024.
- 1010 Smrzka, D., Zwicker, J., Bach, W., Feng, D., Himmler, T., Chen, D., and Peckmann, J.: The
 1011 behavior of trace elements in seawater, sedimentary pore water, and their incorporation
 1012 into carbonate minerals: a review, *Facies*, 65, 47, [https://doi.org/10.1007/s10347-019-0581-](https://doi.org/10.1007/s10347-019-0581-4)
 1013 4, 2019.
- 1014 Smrzka, D., Feng, D., Himmler, T., Zwicker, J., Hu, Y., Monien, P., Tribovillard, N., Chen, D.,
 1015 and Peckmann, J.: Trace elements in methane-seep carbonates: Potentials, limitations, and
 1016 perspectives, *Earth-Science Reviews*, 208, <https://doi.org/10.1016/j.earscirev.2020.103263>,
 1017 2020.
- 1018 Tribovillard, N., du Châtelet, E. A., Gay, A., Barbecot, F., Sansjofre, P., and Potdevin, J.-L.:
 1019 Geochemistry of cold seepage-impacted sediments: Per-ascensum or per-descensum trace
 1020 metal enrichment?, *Chemical Geology*, 340, 1-12,
 1021 <https://doi.org/10.1016/j.chemgeo.2012.12.012>, 2013.
- 1022 Viollier, E., Inglett, P. W., Hunter, K., Roychoudhury, A. N., and Van Cappellen, P.: The
 1023 ferrozine method revisited: Fe(II)/Fe(III) determination in natural waters, *Applied*
 1024 *Geochemistry*, 15, 785-790, [https://doi.org/10.1016/s0883-2927\(99\)00097-9](https://doi.org/10.1016/s0883-2927(99)00097-9), 2000.
- 1025 von Breyman, M. T., Brumsack, H., and Emeis, K. C.: Depositional and Diagenetic Behavior
 1026 of Barium in the Japan Sea, in: *Proceedings of the Ocean Drilling Program, 127/128 Part 1*
 1027 *Scientific Results, Proceedings of the Ocean Drilling Program*,
 1028 <https://doi.org/10.2973/odp.proc.sr.127128-1.168.1992>, 1992.
- 1029 Vuillemin, A., Morlock, M., Paskin, A., Benning, L. G., Henny, C., Kallmeyer, J., Russell, J. M.,
 1030 and Vogel, H.: Authigenic minerals reflect microbial control on pore waters in a ferruginous
 1031 analogue, *Geochemical Perspectives Letters*, 28, 20-26,
 1032 <https://doi.org/10.7185/geochemlet.2339>, 2023a.

- 1033 Vuillemin, A., Vargas, S., Coskun, O. K., Pockalny, R., Murray, R. W., Smith, D. C., D'Hondt, S.,
1034 and Orsi, W. D.: Atribacteria Reproducing over Millions of Years in the Atlantic Abyssal
1035 Subseafloor, *mBio*, 11, <https://doi.org/10.1128/mBio.01937-20>, 2020.
- 1036 Vuillemin, A., Mayr, C., Schuessler, J. A., Friese, A., Bauer, K. W., Lücke, A., Heuer, V. B.,
1037 Glombitza, C., Henny, C., von Blanckenburg, F., Russell, J. M., Bijaksana, S., Vogel, H., Crowe,
1038 S. A., and Kallmeyer, J.: A one-million-year isotope record from siderites formed in modern
1039 ferruginous sediments, *GSA Bulletin*, 135, 504-522, <https://doi.org/10.1130/b36211.1>,
1040 2023b.
- 1041 Wickham, H.: *ggplot2*, 2, Use R!, Springer-Verlag, New York, 260 pp.,
1042 <https://doi.org/10.1007/978-3-319-24277-4>, 2016.
- 1043 Widdel, F., Knittel, K., and Galushko, A.: Anaerobic Hydrocarbon- Degrading
1044 Microorganisms: An Overview, in: *Handbook of Hydrocarbon and Lipid Microbiology*,
1045 Springer, Berlin, Heidelberg, 1997-2021, <https://doi.org/10.1007/978-3-540-77587-4>, 2010.
- 1046 Yergin, D.: *The Prize: The Epic Quest for Oil, Money & Power*, Free Press, ISBN
1047 9781847376466, 2009.
- 1048 Zhang, X., Wu, K., Han, Z., Chen, Z., Liu, Z., Sun, Z., Shao, L., Zhao, Z., and Zhou, L.: Microbial
1049 diversity and biogeochemical cycling potential in deep-sea sediments associated with
1050 seamount, trench, and cold seep ecosystems, *Front Microbiol*, 13, 1029564,
1051 <https://doi.org/10.3389/fmicb.2022.1029564>, 2022.
- 1052 Zhao, R. X., Xue, H. T., Lu, S. F., Greenwell, and Erastova, V.: Revealing crucial effects of
1053 reservoir environment and hydrocarbon fractions on fluid behavior in kaolinite pores, *Chem
1054 Eng J*, 489, <https://doi.org/10.1016/j.cej.2024.151362>, 2024.